isvr Institute of Sound and Vibration Research

Oceanic Bubble Sizing: Measurements and Proposed Studies

T.G. Leighton, A.D. Phelps and M.D. Simpson

ISVR Technical Report No 273

January 1998

University of Southampton

SCIENTIFIC PUBLICATIONS BY THE ISVR

Technical Reports are published to promote timely dissemination of research results by ISVR personnel. This medium permits more detailed presentation than is usually acceptable for scientific journals. Responsibility for both the content and any opinions expressed rests entirely with the author(s).

Technical Memoranda are produced to enable the early or preliminary release of information by ISVR personnel where such release is deemed to the appropriate. Information contained in these memoranda may be incomplete, or form part of a continuing programme; this should be borne in mind when using or quoting from these documents.

Contract Reports are produced to record the results of scientific work carried out for sponsors, under contract. The ISVR treats these reports as confidential to sponsors and does not make them available for general circulation. Individual sponsors may, however, authorize subsequent release of the material.

UNIVERSITY OF SOUTHAMPTON

INSTITUTE OF SOUND AND VIBRATION RESEARCH

FLUID DYNAMICS AND ACOUSTICS GROUP

Oceanic Bubble Sizing: Measurements and Proposed Studies

by

T G Leighton, A D Phelps and M D Simpson

ISVR Technical Report No. 273

January 1998

Authorized for issue by
Professor P A Nelson
Group Chairman

ACKNOWLEDGEMENTS

This work was funded by the Natural Environment Research Council ref: GR3 09992

CONTENTS

LIST OF FIGURES

Page No

ABSTRACT

This report discusses the measurement of the subsurface oceanic gas bubble population. A NERC-funded project has, over the past two years, developed a system which has successfully measured the bubble population *at a point,* deployed both as a buoy in coastal waters, and in the surf zone. This report summarises that work, and proposes future directions for the study. The proposed work has two aims. First, it will extend the previous studies to measure the bubble population through the water column, not simply at a point. Second, it will interpret that information in terms of relevant oceanographic parameters (section 3.3), particularly atmosphere/ocean gas flux.

1. INTRODUCTION

1.1 Applications of bubble sizing

The ability to size and count gas bubbles in liquid has many applications relevant to ocean science, including studies into ambient noise (Wenz, 1962; Longuet-Higgins, 1990), the near-surface acoustic waveguide (Buckingham, 1991; Farmer and Vagle, 1989), the atmosphere/ocean fluxes of mass, momentum and energy (Woolf and Thorpe, 1991; Thorpe, 1982), precipitation (Pumphrey, 1990; Scrimger *et al.*, 1987), diver safety (Belcher, 1980; Leighton *et al.*, 1995; Crum and Mao, 1996), dynamic loading on structures (Peregrine, 1994), sonar occlusion, cavitation inception (Akulichev, 1994), and passive sensing (Buckingham and Epifanio, 1997). Bubble detection is also required for many industrial (e.g. Detsch and Sharma, 1990) and medical (e.g. Tickner, 1982) applications.

Because of the differing compressibilities of the gas and liquid, and the impedance mismatch at the bubble wall, acoustic techniques for bubble detection can be potent. Acoustic techniques are by far the most effective for measuring bubble populations, outclassing for example optical techniques in terms of the accuracy with which a radius can be determined, the insensitivity of the technique to departures from the spherical bubble shape, the sample volume that can be examined, and the ability to detect small bubbles. Notably, measurement of the bubble resonance frequency ν_r facilitates observation of small bubbles, since ν_r increases with decreasing bubble radius, R_0 (Leighton, 1994):

$$\nu_0 = \frac{1}{2\pi R_0\sqrt{\rho}}\sqrt{3\kappa\left(p_0 + \frac{2\sigma}{R_0}\right) - \frac{2\sigma}{R_0} - \frac{4\mu^2}{\rho R_0^2}} \tag{1.1}$$

where ρ is the density of the surrounding liquid, p_0 is the hydrostatic pressure at the bubble wall, σ is the surface tension coefficient at the gas / liquid interface, μ is the shear viscosity coefficient and κ is the polytropic index describing the expansion and compression of the gas within the bubble. Therefore, from a knowledge of its resonant frequency, the size of the bubble can be determined. When driven acoustically at low amplitudes, bubbles behave approximately as single degree of freedom oscillators, with the gas inside contributing the stiffness element and the liquid outside the bubble behaving as the mass element. The damping of the bubble pulsations brought on through to viscous losses at the bubble wall, radiation of acoustic energy into the medium and thermal losses in the expansion and compression of the gas.

1.2 Historical measurements of bubble size

The bubble population in the sea tends in the main to increase with windspeed and decrease with depth below the surface (Thorpe, 1982). Early optical investigations by Blanchard and Woodcock (1957) indicated that most of the bubbles in the near-shore zone have radii less than 100 μm. Kolovayev (1976) was probably the first to catch, photograph and count bubbles below breaking waves in the open sea at wind speeds

of up to 13 m/s, by allowing them to rise onto a transparent plate. The bubbles may however have dissolved on rising (Thorpe, 1982). These early measurements suggested that at depths between 1.5 and 8 m, the most common bubbles were those possessing a radius of around 70 μm, and very few bubbles were greater than $R_0 \sim 300$ μm. Johnson and Cooke (1979) photographed bubbles *in situ* in the sea, using a camera suspended from a surface float at depths of 0.5 to 4.0 m, and windspeed of 8 to 13 m/s, in water of 20-30 m depth. They observed that the distribution of bubble size narrowed with increasing depth, the larger bubbles disappearing. The number of bubbles greater than the minimum size they could detect ($R_0 \sim 17$ μm) also decreased with increasing depth, decaying roughly exponentially over depthscales of order 1 m at windspeeds of 11-13 m/s, such that at a depth of 1.8 m the density of bubbles of a detectable size was 1.56×10^5 m^{-3}. They obtained a modal bubble radius in the size distribution of 40-50 μm. However Walsh and Mulhearn (1987) suggest that the photographic observations lack the resolution to accurately count the smallest bubbles. MacIntyre (1986) suggest that in addition to the lower limit imposed by resolution, there is an upper size limit on the reliable data resulting from poor statistics, so that only the data for bubbles in the range 60 μm $< R_0 <$ 150 μm is reliable.

Medwin (1977), making acoustic observations *in situ* through examination of attenuation at various frequencies, suggests that there is a higher proportion of much smaller bubbles. Medwin and Breitz (1989) confirm that the peak in the size spectrum occurs at a radius less than 30 μm, and Su *et al.* (1988) suggest that the peak is around 20 μm. Farmer and Vagle (1989) deployed an upwardly-pointing four-frequency echo sounder (28, 50, 88 and 200 kHz) to investigate the bubble size distribution. Time-of-flight of reflected acoustic pulses gave a measure of distance, with a 10 cm resolution for vertical samples. The backscattered intensities at the four frequencies for each vertical sample gave point measurements of the bubble population at four specific radii in the range $15 < R_0 < 100$ μm. These were then employed in an iterative calculation to give the size distribution of the whole population. They confirmed that an upper bound on the size spectral peak occurs at $R_0 = 22$ μm, the true peak being closer to 20 μm. Medwin and Breitz (1989) used the variation in Q of several modes of a floating acoustical resonator to determine the bubble spectral size distribution at a depth of 0.25 m below a spilling oceanic breaker. The one-dimensional resonator consisted of a flat transducer facing a reflective plate 126 mm away, so that modes could be set up in the water between these. Bubbly water could flow in readily between the plates from the environment. From resonance broadening measurements for nine specific bubble sizes in the range 30 μm $< R_0 <$ 270 μm, Breitz and Medwin (1989) found an average bubble density of

$$n_b^{\mu}(R_0) = 7.8 \times 10^8 \left(\frac{R_0}{1 \mu m} \right)^{-2.7} \qquad \text{(for } 30\ \mu\text{m} < R_0 < 270\ \mu\text{m)} \quad (1.2)$$

where $n_b^{\mu}(R_0)$ is the number of bubbles per cubic metre per micrometre increment in radius. In the same radius range the maximum bubble density detected was $n_b^{\mu}(R_0) = 1.6 \times 10^9 [R_0 / 1\ \mu\text{m}]^{-2.7}$. Medwin and Breitz (1989) however found that only the larger bubbles in the range 60 μm $< R_0 <$ 240 μm followed a $n_b^{\mu}(R_0) \mu [R_0 / 1\ \mu\text{m}]^{-2.6}$

distribution: the population of smaller bubbles (30 μm < R_0 < 60 μm) decayed with depth as $n_b^{\mu}(R_0)\,\mu[R_0/1\ \mu\text{m}]^{-4}$. A $[R_0/1\ \mu\text{m}]^{-4}$ model distribution fits most of the data obtained by bubble counting reasonably well (1991). The most recent publication on bubble size spectra is contained in an edited work by Leighton (1997).

The authors and co-workers have had considerable success in point measurements of the oceanic bubble population near the surface (< 1.5 m), in high wind speeds (11-15 m/s), and in deep water (using an oceanographic definition). These conditions determine those tests, four in all, of historical data with which the results will be compared.

The Johnson and Cooke (1979) data for 0.7 m measurement depth and 11-13 m/s wind speed is shown in Fig. 1, compared with other historical measurements which are described below. Their data shows a steady increase in the population between ~ 200 μm and 60 μm, which then flattens out until approximately 20 μm (it should be remembered that Walsh and Mulhearn (1987) suggested that the smallest bubbles may have been undercounted in this experiment).

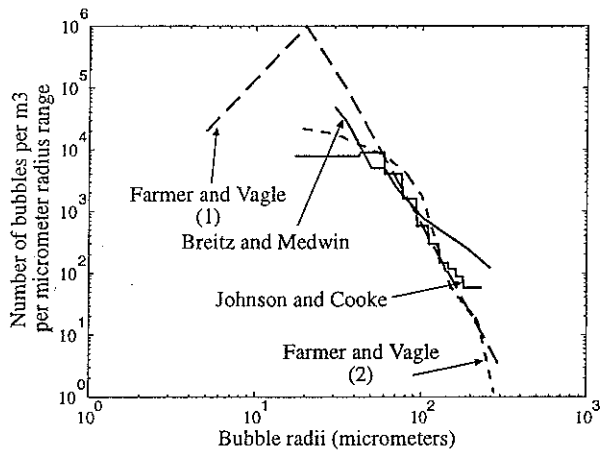

Fig. 1: Comparison of four historical measurements of the near surface bubble population in deep water and at high wind speed. The data is taken from Johnson and Cooke 1979 (unbroken), Farmer and Vagle 1989 (large dashes), Breitz and Medwin 1989 (unbroken) and Farmer and Vagle 1997 (small dashes).

These optical measurements were followed by an acoustic technique of Farmer and Vagle (1989) which used four upwardly facing sonar transducers and monitored the linear backscatter at the four frequencies 28, 50, 88 and 200 kHz. The data was used to infer an ambient bubble population which was then used in modelling the waveguide propagation characteristics in the bubble layer. The population estimates inferred from the strength of the backscattered signal were iteratively matched to the Johnson and Cooke optical data at large bubble size. The estimated population is also shown in Fig. 1, taken at 10 cm depth and in 12-14 m/s wind speed from the Fasinex location, and shows the population to rise up to a maximum at 20 μm of around 1×10^6 bubbles per m^3 per 1 μm radius increment.

The third notable historical measurement was performed by Breitz and Medwin (1989) who used a flat plate resonator to characterise the local oceanic population.

This technique again relies on the linear bubble behaviour to affect the attenuation of modes set up between the two resonator plates, which can be used to infer population numbers for bubbles resonant at those modal frequencies. The technique can yield absolute measures of the bubble population, and their measurements are shown on Fig. 1 with the other two historical estimates. This data was collected at 25 cm below the sea surface in 120 m water depth in a 12 m/s wind speed. Their data shows a monotonically increasing bubble population between 250 and 30 μm, but with a higher number of larger bubbles than the other two estimates and a slightly reduced number of smaller bubbles than those estimated by Farmer and Vagle (1989).

A fourth measurement of the oceanic population is presented again by Farmer and Vagle (1997), who themselves employed an acoustic resonator, but with a larger radius span than the earlier Breitz and Medwin experiment. Their data was taken at a lower depth of 1.3 m, although in wind speeds comparable with the other data shown (10 m/s). Typical data is shown in Fig. 1 with the other historical measurements. The data shows good agreement with the earlier workers for bubbles larger than 40 μm, and then dips off to fall between the Breitz and Medwin data and that of Johnson and Cooke for smaller bubbles. This may be due to the greater depth at which the recent Farmer and Vagle population was measured, or a limitation of their measurement technique. The workers calibrate their data by using their measured population to calculate the sound speed anomaly due to the presence of the bubbles, and compare this directly with measured sound speed data. The agreement is excellent for larger bubbles, but at the smallest bubble sizes there is a divergence between the measured value and predicted estimate.

2. RECENT PROGRESS

2.1 Fundamentals of the generation of combination frequencies

The particular measurements described in these tests uses a combination frequency technique to characterise the bubble population. Here, the bubble population is simultaneously insonified with two sound fields, a *pump* (ω_p) and an *imaging* (ω_i) signal. The pump frequency is a low amplitude signal (for these oceanic measurements at 1000 Pa) whose frequency is varied to coincide with the resonance frequencies of members of the bubble population under investigation (for these oceanic measurements, this ranged between 17 and 200 kHz). The imaging signal is considerably higher in frequency (here set at 1 MHz) and is used to continuously insonify the population. The high frequency backscattered signal is then monitored. For a single bubble, this consists of the geometrically scattered sound from the bubble, brought about by the impedance mismatch at the bubble wall. However, if the pump sound field is at or close to a bubble resonance, the bubble will be pulsating at this frequency, and the target area of the scatterer will therefore be changing. Therefore the backscattered signal will be amplitude modulated at the frequency of the pump signal (Fig. 2), resulting in the generation of sum and difference signals at $\omega_i \pm \omega_p$. Thus the technique monitors the basic linear resonant pulsation characteristics of a bubble through the generation of a nonlinear component in the returned signal.

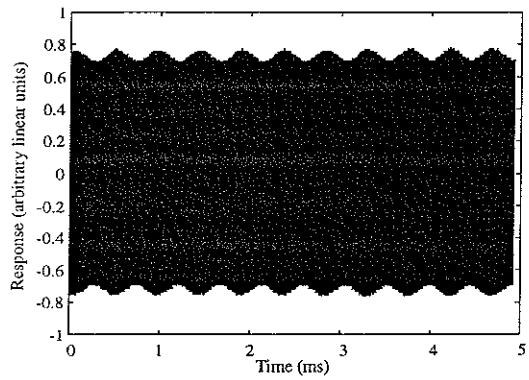

Fig. 2: Returned signals from a bubble insonified at two frequencies measured with a high frequency probe - the high frequency imaging signal was set at 1.1 MHz, and the bubble resonance/pump frequency at 2160 Hz. The data was sampled at 10 MHz on a LeCroy 9314L digital oscilloscope. The pump signal amplitude is 25 Pa 0-Pk. The high carrier frequency plots so densely as to appear black in the figure.

The benefits of using a two frequency technique over a signal frequency insonification measurement are that the analysis of the returned signal allows less ambiguous and more accurate estimates of the measured population. When single frequency linear backscatterers are employed, there is an ambiguity in the returned signal, as a large bubble insonified by a high frequency sound field may scatter more sound than that from a smaller resonant bubble (Fig. 3). However, the height of the combination frequency signal at $\omega_i \pm \omega_p$ is a global maximum at the bubble resonance. This is shown in an earlier paper (Phelps and Leighton, 1997), where a large bubble is insonified by a pump signal three times higher in frequency than the bubble resonance: small sum-and-difference signals are generated, at amplitudes very close to the model predictions, demonstrating the potential to account for off-resonance scattering.

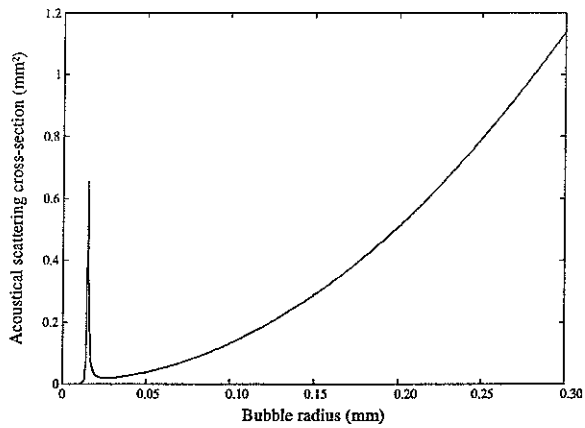

Fig. 3: The calculated acoustic scattering cross-section of a single air bubble in water, as a function of the radius of that bubble, when it is insonified at 20 kHz. The damping is assumed to be constant with a quality factor of Q=15. There is strong scatter from the resonant peak, but also from larger bubbles because of simple geometric effects.

Additionally, there is a considerable improvement in the spatial localisation of a bubble using this technique over single frequency insonification. At resonance, the wavelength of the insonifying sound field is much larger than the bubble radius; for example, a 1 mm radius bubble in water at atmospheric pressure is resonant at

approximately 3.2 kHz, whereas a 3.2 kHz plane wave has a wavelength of about 0.5 m. However, the insonifying volume of the combination frequency measurements is determined solely by the intersection of the high frequency projector and receiver transducers, and is therefore much smaller and easier to calculate accurately. A further benefit of the technique is that the modulation process translates only the relevant bubble mediated information from the 'noisy' frequency window around the resonance (due to the incident acoustic pump signal, bubble entrainment noise etc.) to a much quieter window around the imaging frequency, thereby allowing an improved signal to noise ratio.

Combination frequency measurements have been employed by earlier workers sizing bubbles in the laboratory using increasingly more sophisticated signal processing techniques (Newhouse and Shankar, 1984; Chapelon *et al.*, 1985; Shankar *et al.*, 1986), and once on an oceanic population (Koller *et al.*, 1992). However, the latter tests were concerned only with bubbles resonant between 2.5 and 6 kHz, whereas to fully characterise the ambient population, it is necessary to investigate bubbles up to approximately 200 kHz, as discussed later in section 3.3 (Leighton *et al.*, 1996; Farmer and Vagle, 1997). The workers used a chirped signal as their pump source, and an imaging frequency of 450 kHz, and no distinction was made in their tests between bubble mediated signal coupling and that caused by turbulence and direct reflection of the imaging signal off the moving pump transducer face plate. As will be shown, the contribution to the sum-and-difference signal from this direct coupling is significant, and care must be taken to distinguish and remove this effect from the bubble count. Additionally, the large off-resonant nature of the $\omega_i \pm \omega_p$ signal was ignored by Koller *et al.* (1992) (which is important to include since the volumetric pulsation resonance of a bubble has a significant Q value). Also, Koller *et al.* did not compensate for the variable frequency response of the pump transducer, a necessary step if the amplitude of the sum-and-difference signal components is to be related to bubble numbers.

This report comes at the start of the final year in a NERC-funded research project (grant reference GR3 09992). Before suggesting a future direction for the research, this document describes measurements of the oceanic bubble population during two sea trials. Both employ the combination frequency technique. The first was in the surf zone, where the bubble population at four distinct radii (corresponding to bubbles resonant at pump frequencies of 28, 50, 60 and 88 kHz) are measured (Phelps *et al.*, 1997). The results indicate a local population more than two orders of magnitude higher than any of the deep water measurements, as a result of the greatly increased wave breaking activity in the shallow water.

The second trial, a buoy-deployment, was in water of 20 m depth for high wind speeds (10-12 m/s). The number of bubbles at ten distinct radii ranging between 192 μm and 16 μm were estimated at a depth of 0.5 m. The apparatus, the calibration procedure, and the method of obtaining bubble counts from the acoustic data, were all improved between the two tests. These developments are described below. The results are compared with historical measurements and differences in the bubble size spectra discussed.

2.2 Calibration

2.2.1 Calibration theory

There are several stages in the calibration of the system which are necessary to successfully deploy the combination technique. These are described in detail in the references (Phelps and Leighton, 1997; Phelps *et al.* 1997), and involve several stages, including ensuring that the acoustic field within the sensing volume is well-known. The most significant work in the calibration stage, however, has been in the conversion of the acoustic signal detected from the bubble into measurements of the bubble population itself.

It is a requirement of a generalised bubble sizer that it be able to get an absolute measure of the population, rather than relying on existing data as a starting point for an interpolation procedure. The procedure for translating the measured spectral levels into an absolute bubble counts are outlined below, and involves employing a suitable model for the bubble pulsation response to two frequency insonification.

The calibration procedure is as follows. A stream of single size rising bubbles was insonified in the laboratory using the same apparatus as would be later employed in the sea trials. Using the same experimental set-up for both sets of tests enables several parameters in the pulsation modelling to be poorly defined without any loss of accuracy in the eventual calculations, such as the amplitude of the imaging signal and the distance between the receiver transducer and the transducer focus. Having obtained measured voltage levels for the various spectral components of the returned signal, the same insonification conditions as those used in the experiments were modelled to estimate the expected sound pressure levels at the different returned signal frequencies. A comparison between the measured and modelled signal heights allows a transfer function relating the measured voltage levels to the actual number of bubbles to be estimated. The modelled signal heights for the ten frequencies used in the sea trials were then estimated (using parameters relevant to sea water). These were then used, along with the estimated transfer function and measurements of the frequency response of the components in the returned signal line, to obtain bubble population estimates from measured two frequency backscattered signal levels.

The first attempt at converting combination-frequency data into bubble numbers was made by Zabolotskaya and Soluyan (1973) and Newhouse and Shankar (1984), who analytically derived expressions for the height of the sum-and-difference terms using simplified forms of the Rayleigh-Plesset equation to obtain expressions for the pressure amplitudes at the various frequency locations. However they took account only of viscous damping of the bubble motion, which is an order of magnitude smaller than damping through thermal and radiation losses (although it should be noted that Newhouse and Shankar made the damping an unknown variable which they optimised to give best fit between their measured data and the bubble counts they expected). Neglect of thermal damping in this way can lead to errors of 31 dB (see section 2.4). This error was reduced to around 1 dB for the first sea trial by including radiation and thermal effects explicitly by introducing extra terms into the Rayleigh Plesset equation. The procedure was further refined for the second sea trial by employing a

bubble pulsation model based on the formulations derived by Herring (1941) and Keller and Miksis (1980). These two approaches are now detailed.

A corrected form of the Rayleigh-Plesset equation is used as a starting expression, which includes an extra term which has been shown to give a reliable measure of the dissipative effects of sound radiation through a compressible medium (Neppiras, 1980). Additionally, the thermal conduction into the fluid is included in an approximate manner by assuming that the pulsations behave polytropically, with an index κ calculated theoretically using the expressions of Eller (1970). The modified form of the Rayleigh-Plesset differential equation is:

$$\rho R\ddot{R}+\frac{3}{2}\rho\dot{R}^2=p_B(t)-p_0-P(t)+\frac{R}{c}\left(1-\frac{\dot{R}}{c}\right)\frac{dp_B}{dt} \qquad \text{(2.1)}$$

where R is the instantaneous bubble radius with its two derivatives with respect to time indicated with dots above the character, c is the speed of sound in the liquid and $P(t)$ is the acoustic driving term. The remaining term $p_B(t)$ is a measure of the pressure immediately outside the bubble wall, and represents the forcing term on the liquid due to the bubble which the acoustic pressure has to overcome. It is given by:

$$p_B(t)=\left(p_0+\frac{2\sigma}{R_0}\right)\left(\frac{R_0}{R}\right)^{3\kappa}-\frac{2\sigma}{R}-\frac{4\mu\dot{R}}{R} \qquad \text{(2.2)}$$

Following the methodology of the earlier workers, an approximate solution to this expression is sought by considering a small radial perturbation, where the variable R can be re-written in terms of a displacement variable x as:

$$R=R_0(1+x) \qquad \text{with} \quad x<<1 \qquad \text{(2.3)}$$

Using this substitution, and neglecting all terms beyond those in x^2, equation (2.1) can be re-written as:

$$\begin{aligned}
&\rho R_0{}^2(1+x)\ddot{x}+\frac{3}{2}\rho R_0{}^2\dot{x}^2=\left(p_0+\frac{2\sigma}{R_0}\right)\left[1-3\kappa x+\frac{3}{2}\kappa(3\kappa+1)x^2\right]-\\
&\left[p_0+\left(\frac{2\sigma}{R_0}\right)\left(1+x+x^2\right)\right]-4\mu\left(\dot{x}-x\dot{x}\right)+p_1\cos\omega_1 t+p_2\cos\omega_2 t+\\
&\frac{R_0}{c}\left\{3\kappa\dot{x}\left(p_0+\frac{2\sigma}{R_0}\right)\left(3\kappa x+\frac{R_0}{c}\dot{x}-1\right)+4\mu\left(\dot{x}^2-\ddot{x}+\frac{R_0}{c}\dot{x}\ddot{x}\right)+\right.\\
&\left.2\sigma\dot{x}\left(\frac{1}{R_0}-\frac{x}{R_0}-\frac{\dot{x}}{c}\right)\right\}
\end{aligned} \qquad \text{(2.4)}$$

where ω_1 and ω_2 are the two angular frequencies of the sinusoidal driving sound fields and p_1 and p_2 are their corresponding pressure amplitudes. If the acoustic radiation terms (shown grouped in curly brackets) are removed by considering the incompressible case of $c \rightarrow \infty$, this equation becomes equation (5) from Newhouse and Shankar's 1984 paper. The subsequent analysis follows the method in the earlier paper of writing a solution to the displacement variable x in terms of the sum of radial excursions at ω_1, ω_2, $2\omega_1$, $2\omega_2$, $\omega_1+\omega_2$ and $\omega_1-\omega_2$, substituting this into the modified Rayleigh-Plesset equation, and then equating the terms at the various different frequencies. The analytical solution is readily obtained (but cannot be simplified to obtain a transparent expression of the form obtained by Newhouse and Shankar, 1984, and is therefore not presented here), and its use is described in the next section. It is the case, however, that the results for the radiated pressures at the sum-and-difference frequency locations is numerically equal to those obtained by augmenting the damping term given in equation Newhouse and Shankar's equation (8) with the expression for the non-dimensional radiated damping coefficient presented by Eller (1970). If the more general off-resonance form for the viscous damping is employed, then their variable δ can be replaced with the general damping parameter d_{tot}, given by:

$$d_{tot} = \frac{4\omega_2 \mu}{3\kappa p_0} + \frac{\rho}{3\kappa p_0}\frac{(R_0\omega_2)^3}{c} \tag{2.5}$$

where ω_2 is considered to be the angular frequency of the pump sound field.

This procedure was further improved for the second sea trial by using the model of the bubble pulsation characteristics based on the formulations derived by Herring (1941) and Keller and Miksis (1980), and can be written as:

$$\left(1-\frac{\dot{R}}{c}\right)R\ddot{R}+\frac{3}{2}\dot{R}^2\left(1-\frac{\dot{R}}{3c}\right)=\left(1+\frac{\dot{R}}{c}\right)\frac{1}{\rho}\left[p_B(t)-p_0-p\left(t+\frac{R}{c}\right)\right]+\frac{R}{\rho c}\frac{dp_B(t)}{dt} \tag{2.6}$$

where the symbols are defined earlier. Using the same substitution detailed in equation (2.3), it is possible to re-write equation (2.6), where all terms beyond those in x^2 are neglected (Phelps and Leighton, 1998, calculated x and demonstrated that the expansion of equation (2.6) is valid, as is the neglection of terms higher than x^2).

Because this refined analysis includes for a finite speed of sound in the medium, rather than assuming the surrounding liquid to be incompressible as is the case with the Rayleigh-Plesset expansions, its explicitly allows for energy losses through acoustic radiation into the medium. By again incorporating a polytropic relationship which relates the pressure of the gas inside the bubble to the radius, rather than the earlier adiabatic relationship assumed by earlier workers, the thermal damping losses are also considered. The value of κ is again calculated theoretically using the expressions of Eller (1970).

2.2.2 Calibration results

In addition to changing the processing algorithm between the two trials, as discussed in the previous section, the hardware was also modified. The surf zone trial was moored, whilst the second test (in 20 m of water) was buoy-deployed. Perhaps most importantly, the focus of the high-frequency transducers was enlarged, increasing the sensing volume from 0.2 ml to 1 ml, and dramatically decreasing the error arising from the uncertainty associated with this volume (see Phelps *et al.* 1997; Phelps and Leighton 1997; Leighton *et al.*, 1997). The sensing volume was calculated by modelling the beam patterns of the two high frequency transducers by performing a Rayleigh integral over their surfaces. When these patterns were overlapped in the same layout as the transducer arrangement, they allowed the insonification volume to be estimated. This gave the sensing volume, defined by where the sensitivity fell off to 3 dB of its maximum value. The beam overlap for the transducer geometry employed in the buoy-deployment is shown in Fig. 4, where the distance between both the high frequency transducers and the focus is 16 cm and both transducers are angled at 45 ° to the vertically rising bubble flow.

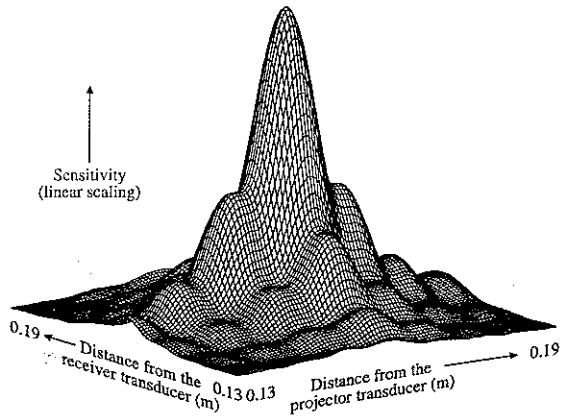

Fig. 4: The sensitivity within the sampling volume, for the geometry employed in the Channel test.

Nevertheless the equipment schematic shown in Fig. 5 is roughly valid (for example, the 200 m cable was not buried for buoy-deployment) for both of the oceanic tests, and for the calibration which took place prior to each sea trial. To ensure that any potential signal corruption was identified and compensated for, the laboratory tests employed the apparatus exactly as it would be used in the later oceanic tests, although without the equipment canister (described later), and at the same anticipated transducer depth (which was ~1.5 m for the surf zone test, and 50 cm for the buoy-deployment). The frequency response of the pump transducer was previously calibrated over the frequency range employed in all the tests, allowing constant and known insonification conditions to be employed.

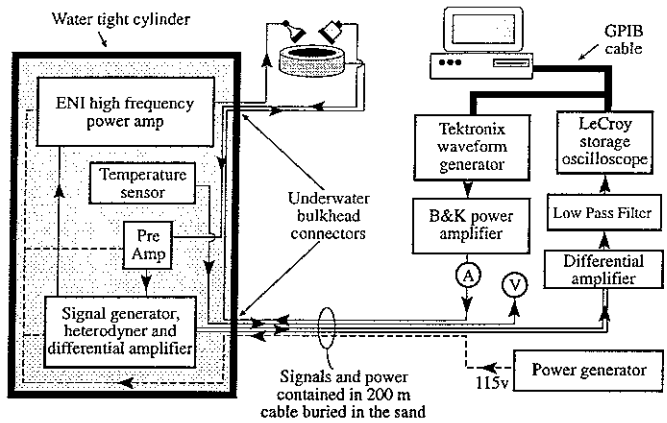

Fig. 5: Schematic of the apparatus used in the surf-zone trial

The historical manner for presenting the bubble population information is as the number of bubbles at a particular bubble radius per cubic meter of water per micrometer radius range. Thus it is important to be able to determine the radius range over which the sum-and-difference signals persist, so this can be compensated for in the analysis. This was again achieved through the Herring-Keller simulations, where the radial width of each sum-and-difference peak was taken as the radius span before the signal height dropped by 3 dB.

2.3 Results of laboratory tests

A steady stream of similar size bubbles was used in the laboratory tests, generated by passing compressed air through a hypodermic needle which had been constricted at the tip - the large pressure drop at the tip ensured that the bubbles would all be the same size (Clift *et al.*, 1978). Fig. 6(a) shows a typical returned signal from the insonification of the laboratory bubble stream for a pump frequency of 4.8 kHz and at 200 Pa amplitude. This pressure amplitude is smaller than that used in the later sea trials, as it was found that this was the maximum insonification level before surface waves were excited on the bubble wall (Phelps and Leighton, 1996), which caused the rising bubbles to follow a helical path rather than a vertical path through the high frequency transducer focus. Clearly visible are the $\omega_i+\omega_p$ and $\omega_i-\omega_p$ signals separated by approximately 600 Hz - this is evident because the scattered signals are subjected to a Doppler shift due to the bubble movement. To facilitate the information transfer and storage, the high frequency signal scattered from the bubble is analogue demodulated using the original imaging signal (described elsewhere - Phelps *et al.*, 1997), and the two peaks are shifted accordingly. The demodulated and Doppler shifted imaging signal is also evident at 300 Hz.

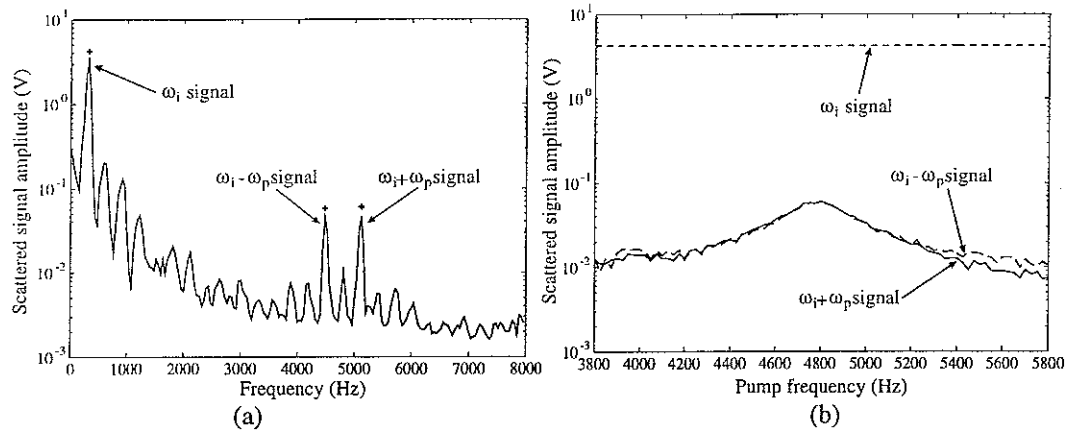

Fig. 6(a): Typical spectrum from laboratory measurements at $\omega_p/2\pi$ = 4.8 kHz. The data was insonified at a pump signal amplitude of 200 Pa, and the crosses indicate the heights of the signals after the energy summation at each of the peaks. Fig. 6(b): Heights of the sum-and-difference signals (unbroken and large dashes respectively) and imaging signal (small dashes) when the stream of bubbles resonant at 4.8 kHz are insonified between 3.8 and 5.8 kHz in discrete 25 Hz steps, and at an amplitude of 200 Pa.

Fig. 6(b) records the 'height' of the imaging and the sum-and-difference peaks, as the laboratory bubble stream was insonified with a pump signal of amplitude 200 Pa between 3800 Hz and 5800 Hz in 25 Hz steps, a frequency interval within which the bubble resonance is known to lie. These signal 'heights' were found through FFT-ing the returned data, and then summing the energy over each peak. This was then converted back to a voltage measurement, as it was found that this gave the most accurate and constant signal height estimates. In summary, therefore, the crosses shown above the three peaks in Fig. 6(a) indicate this equivalent signal voltage for a single setting of the pump frequency, whilst the data in Fig. 6(b) shows the three signal heights over the entire range of pump signals. It is apparent that the bubbles in the stream are resonant at 4.8 kHz, with a returned signal height of 0.060 V at the location of the $\omega_i+\omega_p$ signal and 0.058 V at the $\omega_i-\omega_p$ signal. The imaging signal remains constant over the series of measurements, at a height of 4.15 V. This gives a ratio of the imaging signal to the $\omega_i+\omega_p$ signal of 36.8 dB and of 37.1 dB to the $\omega_i-\omega_p$ signal, which can be used to validate the performance of the model later on.

The second stage of the calibration involved modelling the bubble-mediated sound pressure at the receiver transducer due to the two insonifying sound field signals. The same bubble size and insonification conditions as employed in the laboratory experiments were used, for a range of bubble sizes from 600 to 800 μm insonified by a 200 Pa amplitude sine wave of frequency 4800 Hz. The results from estimating the height of the two $\omega_i\pm\omega_p$ signals and the ω_i signal are shown in Fig. 7.

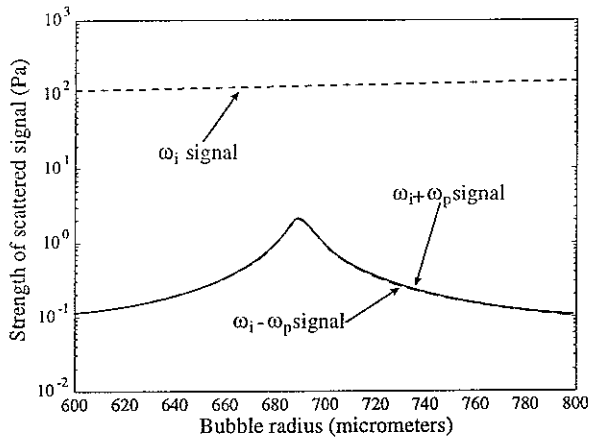

Fig. 7: Analytically derived amplitudes of the sum-and-difference signals (unbroken and large dashes respectively) and imaging signal (small dashes) for an insonifying sound fields of frequency 4.8 kHz and an amplitude of 200 Pa, over a radius range 600 - 800 μm.

It is clear from Fig. 7 that the strengths of the signals at $\omega_i+\omega_p$ and at $\omega_i-\omega_p$ reach maxima of 2.13 Pa and 2.05 Pa respectively at a bubble radius of 689 μm, with a height of the scattered imaging signal of 129 Pa. The 3 dB width of the peak can also be estimated at 9.9 μm. This can be now compared with the measurements of the scattered signal from the 4800 Hz bubble stream. Comparison of the heights of the two imaging signal strengths, and consideration of the frequency responses of the preamplifier and demodulator, allow the sensitivity of the high frequency transducer to be estimated at 8.8 μV/Pa.

As a method of testing the validity of the model, the difference in the strengths of the imaging signal and the two sum-and-difference peaks were also calculated. The ratio of the imaging signal to the sum and difference terms is 35.7 dB and 36.0 dB respectively in the theoretical predictions, which results in a 1.1 dB discrepancy in both cases when compared to the experimentally measured difference shown in Fig. 6(b). This is equivalent to a 14 % error in the estimates of the sum and difference signal pressure. If the damping was taken to comprise viscous losses alone, and the thermal and radiation effects were to be ignored (see section 2.2.1), the ratio of the imaging signal height to that of either combination frequency signal would be less than 1 dB, which is equivalent to a discrepancy of ~ 35 dB. A further validation of the off-resonance behaviour is achieved through a comparison of the two Quality factors of the theoretical and experimental data. If, as a first approximation, the resonance frequency is considered to be inversely proportional to the bubble's equilibrium radius (as is the case when using Minnaert's 1933 publication to relate the two parameters), the Q factor of the theoretical signal heights can be estimated from the ratio of the radius spread of the sum-and-difference signals, to their resonant radius value. This gives a Q factor of 18.2, which compares very closely with the value of 17.8 measured from the experimental data.

2.4 Sea trials

2.4.1 Results from the surf zone

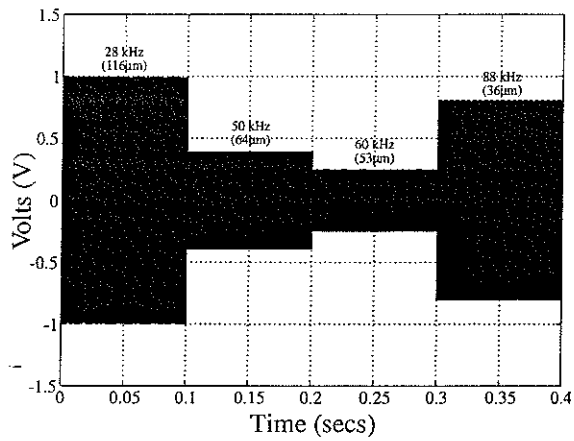

Fig. 8: The electrical signal supplied to the ring transducer for the surf zone trials. The pulse contains four tones, delivered consecutively, each lasting 0.1s, at 20, 50, 60 and 88 kHz. The sinusoids within the pulse plot so densely as to appear black.

The ring transducer generates a pulse which consists of four consecutive tones. The electrical signal to the ring transducer is shown in Fig. 8, where the amplitude for each of the four tones is corrected for frequency response of the transducer system, such that the acoustic pressure amplitude in the focus is a constant 3000 Pa for all four frequencies.

The equipment, shown in schematic in Fig. 5, was deployed in the rig shown in Fig. 9. It was placed at low tide on the shored line, to be covered by the sea as the tide came in (Fig. 10 shows the equipment set-up uncovered at low tide). Data was collected once the rig was fully submerged, the sensing volume being at a depth of ~1.5 m. The canister comprised a 1000 mm long × 355 mm diameter watertight aluminium alloy cylinder, which was painted to minimise corrosion and clamped to a rigid scaffold as shown in Fig. 9. The canister contained the high frequency projector signal power amplifier, the crystal oscillator, high frequency receiver preamplifier, demodulator equipment and the first of the differential amplifier pair (to ensure that there was no signal corruption in the passage of the returned signal along the 200 m umbilical connecting the canister to the shore-based equipment). Additionally a temperature sensor was added to monitor the effects that the enclosed space had on the potential of the equipment to overheat.

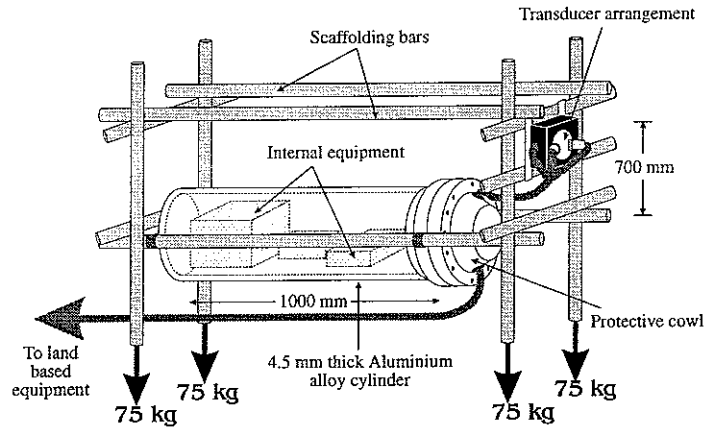

Fig. 9: The arrangement of the cylinder for the North Sea test

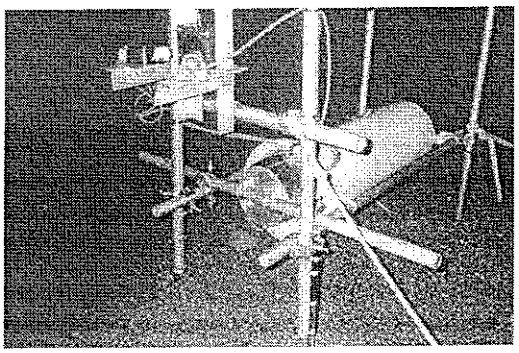

Fig. 10: Photograph of the apparatus set-up at low tide during the North Sea test.

Fig. 11 shows the time-averaged bubble counts at the bubble radii of 120, 66, 55 and 37 μm. A +200% and -50% error is associated with each data point arises primarily from the uncertainty associated with the sample volume: other sources of error are considered by Phelps *et al.* (1997) and found to be much less significant.

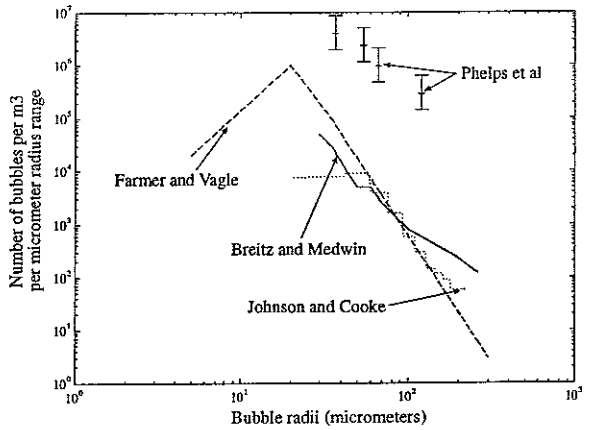

Fig. 11: The bubble counts (the time-average of the data shown in Fig. 12) for four pump frequencies (20, 50, 60 and 88 kHz), equivalent to bubble radii of 120, 66, 55 and 37 μm. The bubble size is plotted against the number of bubbles per cubic metre per micrometre increment in radius. Also shown are the data of Breitz & Medwin (1989), Farmer & Vagle (1989) and Johnson & Cooke (1979).

The time-average is taken over the data shown in Fig. 12, which shows the time-resolved bubble counts found in the North Sea test. This degree of time-resolution is possible since the data is collected in a series of 0.4 s 'snap-shots', rather than requiring the time-averaging inherent in earlier studies. It should be noted that on occasions during the analysis the signal height peaked below the noise floor, and in these cases the particular readings have been left as gaps. In general, the smaller bubbles are the most populous. Certain correlations between the counts of the various bubble sizes do appear at times (e.g. 120-180 s in (a); 20-40 s in (c)), although in the absence of other measurements there is no way of knowing the time-scales on which the population varies, and therefore whether any aliasing occurs.

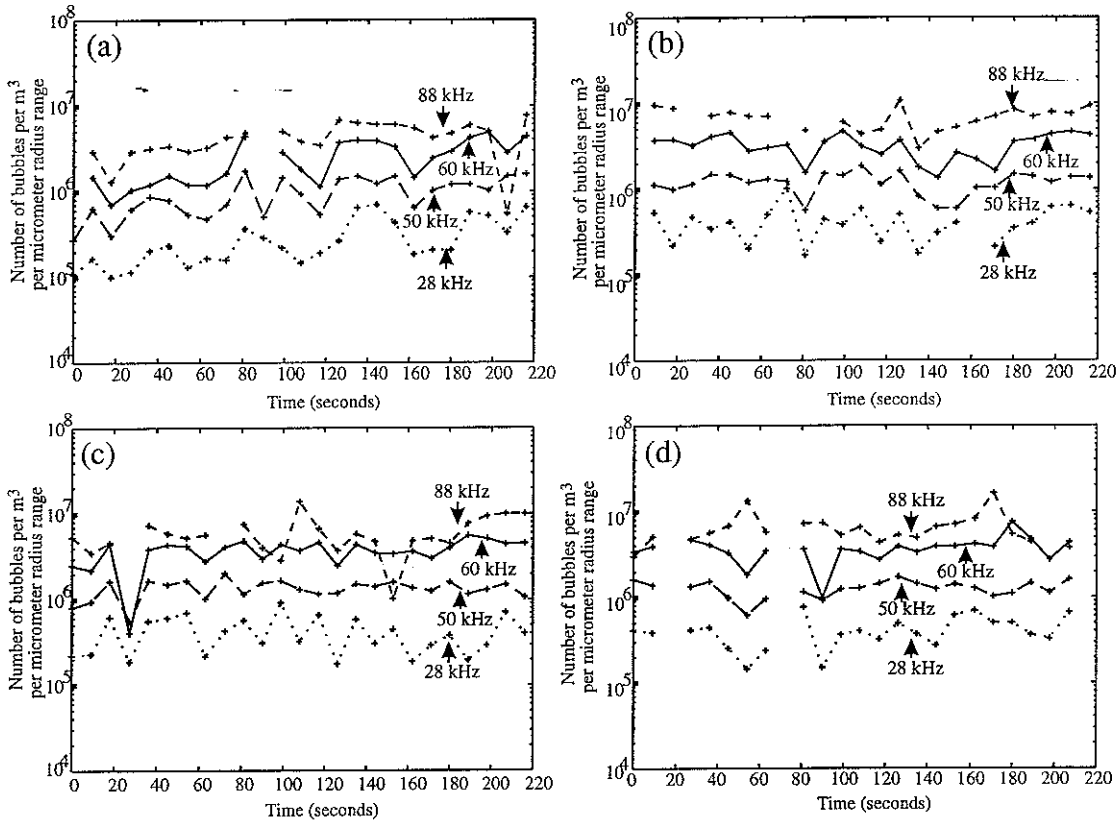

Fig. 12: The time-resolved bubble population densities, resonant at 28, 50, 60 and 88 kHz (i.e. of radius 120, 66, 55 and 37 μm respectively), measured at starting times of (a) 22.00, (b) 22.30, (c) 23.00 and (d) 23.30 GMT on 5 November 1995 in the surf zone at Tunstall. The error associated with each point is +200% and -50%. Some data points in the consecutive tests are missing. The bubble density is expressed in terms of the number of bubbles per cubic metre having a radius within a 1 μm range about the radius given.

2.4.2 Results from the buoy-deployed rig

The ring transducer generates a pulse which consists of ten consecutive tones. The electrical signal to the ring transducer is shown in Fig. 13, where the amplitude for each of the ten tones is corrected for frequency response of the transducer system, such that the acoustic pressure amplitude in the focus is a constant 1000 Pa for all ten frequencies. The pump signal contained ten frequencies at 17, 28, 50, 60, 88, 110, 145, 165, 180 and 200 kHz (corresponding to resonant bubble radii of 192, 157, 64,

53, 36, 29, 22, 20, 18 and 16 μm), which were concatenated into one signal with suitable markers to speed up the data collection and storage.

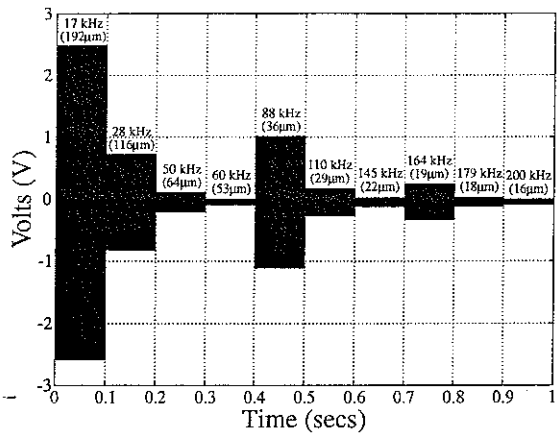

Fig. 13: The electrical signal supplied to the ring transducer for the buoy-deployment. The pulse contains ten tones, delivered consecutively, each lasting 0.1s. The pump signal frequencies were at 17, 28, 50, 60, 88, 110, 145, 165, 180 and 200 kHz (corresponding to resonant bubble radii of 192, 157, 64, 53, 36, 29, 22, 20, 18 and 16 μm). The sinusoids within the pulse plot so densely as to appear black.

The equipment schematic for the oceanic trials is shown earlier (Fig. 5). The same canister as for the surf-zone tests was used, this time deployed from a buoy (Fig. 14), with the 200 m umbilical connecting the canister to the ship-based equipment. The ring transducer, which was now placed with its axis vertical, was deployed at 50 cm below the surface (Fig. 15).

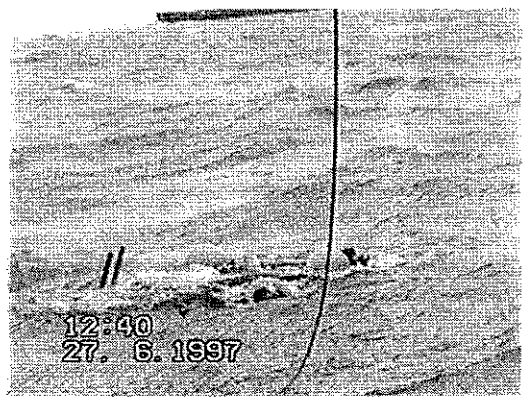

Fig. 14: One frame from the video of the buoy-deployment

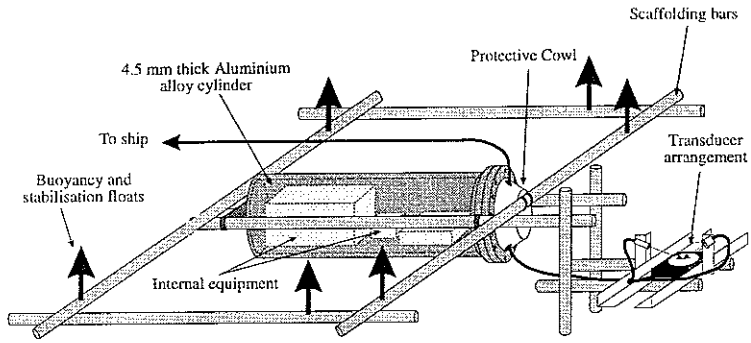

Fig. 15: Deployment details of the watertight canister and buoy.

The buoy was deployed from the back of a ship and allowed to drift 30 m behind the vessel. The wave events around the apparatus were continuously videoed (Fig. 14) to allow the measured bubble population to be tallied up with the sea state during analysis, and the variation in wind speed and water depth were noted throughout. Additionally, a Dictaphone record of the measurements and a slide film was taken, again with the time of each shot noted for later population comparisons.

The tests were performed on 27th June 1997 in water whose depth ranged from 17 m to 22 m and in (un-seasonally high) wind speeds between 10 - 12 m/s, gusting at up to 16 m/s. The equipment was deployed off the Southampton coast at 50° 46.153' N, 1° 80.911' W. The backscattered sound at each separate frequency was sampled at 500 kHz for 50,000 points, which resulted in a 1 second sample window of the bubble population over the ten output signals. The bubble population was insonified at 1000 Pa pump signal output, which is suitably low amplitude to ensure that the small perturbation approximations inherent in the analytical model are valid, and that the insonifying sound field does not affect the local population through rectified diffusion (Leighton *et al.*, 1996).

A typical returned signal from the tests is shown in Fig. 16. To facilitate the data processing, the returned data was digitally narrow band filtered, decimated and the largest frequency component of the signal (the un-shifted main peak due to direct scattering of the imaging signal from the moving pump transducer itself) removed to improve the signal to noise ratio. Thus the frequency axis shows a scale centred around 1000 Hz regardless of the value of the pump frequency, although the relative frequency scale is still correct. Clearly visible are the two signals at $\omega_i \pm \omega_p$, which have undergone a Doppler shift when being scattered from a moving bubble, and are located 500 Hz either side of the direct coupled signal at 1 kHz.

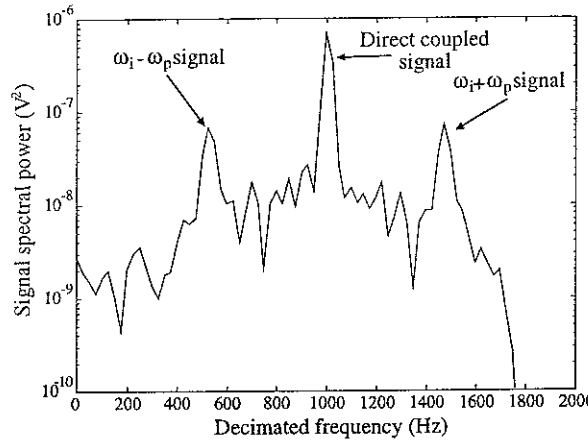

Fig. 16: Typical results from the oceanic measurements, showing the demodulated, filtered and heterodyned frequency content for an insonifying 110 kHz pump signal. The frequency axis shows a scale centred around 1000 Hz regardless of the value of the pump frequency, although the absolute frequency difference of signals around this direct coupled sum-and-difference peak frequency are still maintained.

The analysis of the measured signal strength involved summing the energy over each of the peaks and converting this total signal energy estimate back to a voltage sum, as described earlier in keeping with the laboratory calibration tests. The energy summation was performed automatically, with often more than one bubble contributing to the total $\omega_i \pm \omega_p$ energy. The criteria for deciding whether a signal is bubble mediated is that there must be a simultaneous peak in the spectrum at the same frequency distance from the direct coupled signal, and the signal energy of the two peaks must be within a factor of two. This analytical procedure will inevitably include some non-bubble information into the final count, but will also ensure that bubbles which pass through the transducer focus for a short period of time (as most will compared with the 0.1 s sample window at each frequency) will also contribute to the total bubble count.

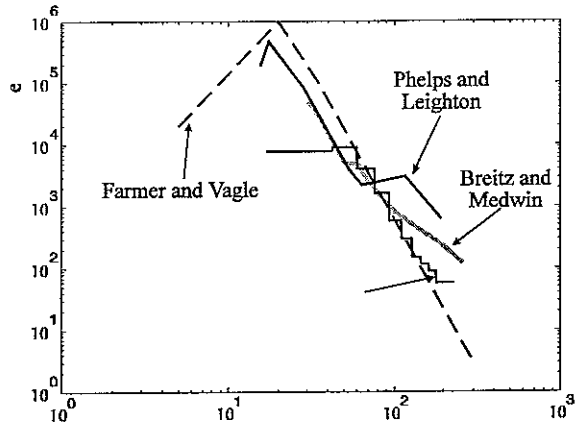

Fig. 17: Comparison of measurements of the near surface bubble population. The data is taken from: Johnson and Cooke (1979, unbroken line); Farmer and Vagle (1989, large dashes); and Breitz and Medwin (1989, unbroken). Also shown are the combination-frequency data taken by the author and co-workers in the Solent (large, unbroken line, the data being from taken from the last of 6 trials taken that day).

In total, six tests were performed, each comprising of ten consecutive runs of the ten frequency signal. The runs were 8 seconds apart, caused by the time required to transport all the data across to the PC via the GPIB interface. These results were then analysed to get the total bubble mediated voltage signal at both the $\omega_i+\omega_p$ and $\omega_i-\omega_p$ frequency locations. These were corrected with the estimate for the sensitivity of the receiver transducer and the measured frequency responses of the preamplifier, demodulator and differential amplifiers to get a measured bubble sound pressure level. This was converted into the number of bubbles per micrometer radius range by dividing the estimates through by the theoretical 3 dB spreads of the $\omega_i+\omega_p$ and $\omega_i-\omega_p$ signals (this has been shown to yield an accurate estimate for the off-resonant bubble contribution - Phelps and Leighton, 1997), and scaled to give the number per unit volume by dividing by the estimated insonification volume. The average bubble density was then calculated by averaging over the ten time samples which made up the test, and by averaging the estimates derived from the sum and difference data. At smaller radii, the theoretical heights of the $\omega_i+\omega_p$ and $\omega_i-\omega_p$ signals begin to diverge, probably due to the truncation of the expanded Herring-Keller series at terms in x^2. This tends to over-estimate the number of bubbles using the $\omega_i-\omega_p$ signal and under-estimate the population using just the $\omega_i+\omega_p$ signal, and thus an average should be a better indicator of the actual population. The estimated average population for a typical test is shown in Fig. 17, compared with historical measurements.

It is apparent that the size spectrum estimated using this two frequency technique yields a similar form to the earlier measurements, but differs slightly in several important respects. For bubbles larger than 80 μm radius, the combination frequency tests show a considerable increase in population over any of the historical studies. This may be a result of wave action against the buoy generating larger bubbles, but it is unlikely to be an artefact of the measurement procedure as any systematic error (such as a mistake in the estimation of the receiver transducer sensitivity or the measurement volume) would be evident over the entire range. Between 30 and 80 μm radius, the data follows the Breitz and Medwin estimates very closely down to the size resolution limit of their data collection. For bubbles smaller than 30 μm, the combination frequency population data carries on rising to a peak of 5×10^5 bubbles per m^3 per micrometer radius range at 18 μm radius. This is similar to the first Farmer and Vagle (1989) data set, which showed a peak at 20 μm radius of 1×10^6 bubbles per m^3 per micrometer radius range.

As the collected data consists of effective 'snap-shots' of the local bubble population, the time variation of the population can be investigated. Fig. 18 shows a mesh plot of the evolution of the population over the series of individual 'snap-shots' which made up the same test shown averaged in Fig. 17. The mesh plot also shows two of the earlier historical measurements (Brietz and Medwin, 1989; Farmer and Vagle, 1989) at time zero for comparison. It is evident at 24 seconds that a wave break event has just occurred and there is an increase in the bubble population over the entire radius range. A similar, but smaller event, is shown after 56 seconds. In between, the population falls off over the radius range, with a rise in the number of larger bubbles evident at 40 seconds. This evolving population can be matched up with breaking wave events around the apparatus monitored on the video footage, but to date no exact matching has been demonstrated between the two. This is probably due to the depth of

the transducers at 50 cms, which would give a time lag between the wave breaking and the measurements, and the turbulent nature of the sea state, which would move the entrained bubble population through the transducer focus after a random time period which would be impossible to accurately correlate with the wave breaking events.

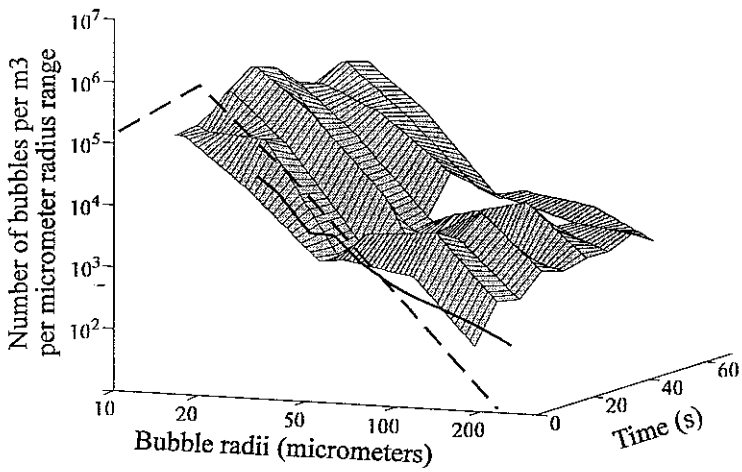

Fig. 18: Mesh plot showing the variation in bubble population over the course of the same trial (no. 6) as the time averaged data shown in Fig. 17. The 'snap-shots' were collected approximately 8s apart, and three historical measurements of the population are shown at time 0 for comparison. Specifically, these time-zero data are from Breitz & Medwin (1989, solid), Farmer & Vagle (1989, dashed). The white region around 48s corresponds to a run when, in a limited radius range, no data was recorded.

A critical examination has been made of the sources of random and systematic uncertainty in the combination-frequency measurement system (Phelps and Leighton, 1998). These may arise through systematic errors in the calibration technique, measurement errors or errors in the analysis of the data itself. The error of 1.1 dB, discussed in section 2.4, in the fit between the bubble pulsation model and the calibration experiment, translates to an overestimation of the population of 14 % in the bubble population, and it is anticipated that this is the greatest source of systematic error in the measurements. Other sources of error are as follows. First, incorporating the thermal damping loss mechanism into the pulsation model by using a polytropic index to represent the compression of the gas inside the bubble is a non-exact description of the actual process. Second, the bubble pulsations are may not be sufficiently low amplitude to be represented in terms of a radial excursion variable (x). Third, there is an uncertainty associated with the estimate of the insonification volume, though this was greatly reduced between the two trials reported in sections 2.4.1 and 2.4.2 (it was the main source of uncertainty in the surf zone trial). Fourth, multiple bubble interactions can be assessed for the low void fraction measured (~ 2.2×10^{-4} %), as can the effects of attenuation and directionality in the high frequency beam. Fifth, the directionality in the scatter of the high frequency signal from the bubble. All these factors are assessed, and the error from each minimised (for example, through careful calibration procedures) and quantified for incorporation into the published reports of the studies. The procedures are involved, and will be reported in Phelps and Leighton (1998).

3. FUTURE WORK

During the progress of the current NERC funded grant, bubble populations have been measured from a moored submerged rig in the surf zone, and in 20 m of water through buoy-deployment. The first trial showed significant advances over recorded measurements, being the first measurements of the bubble size distribution in the surf zone, and the first use of the combination-frequency technique where adequate corrections for damping were included *a priori* in the calibration. For the buoy-deployment, the sources of error were greatly reduced, and the size range and number of bubble radii examined were increased. In both trials the measurement was absolute, and did not require the use of historical measurements against which to fit the data, As time progresses and the requirements for accuracy in higher-density populations increases, this nonlinear technique represents perhaps the least ambiguous way of measuring bubble populations.

Having made such progress, two areas into which the work should be extended are clear. First, the measurements are restricted to a single point (the focus, as illustrated in Fig. 4). Second, the research must now be extended to more directly probe the oceanographic issues for which knowledge of the bubble population is a requirement. These are discussed in the following two sections.

3.1 Adaptation of the apparatus for measurements down and across the water column

The combination frequency systems described in the previous section produce accurate, time-resolved measurements of the bubble population *at a specific point.* It will be possible to adapt these systems to generate a measurement of the population along the line which passes through the central axis of the ring transducer. Hydrophones will be placed along this axis. As the ring transducer produces its pulse (similar to Fig. 13), then each pulse will not only be used to generate the required pump signal at the transducer focus for use in the combination-frequency tests, but will also propagate outwards, to be detected by the hydrophones. That propagation characteristic will then be inverted to determine the bubble population on axis. Such inversions have been performed before (there are, for example, the sound speed and attenuation inversions employed by Melville *et al.* (1997); these were undertaken at 6.5 m depth inshore of the surf line, and so were not included in the comparison of Fig. 17). However in the proposed system the combination-frequency results will be used to give the bubble population at a point along the propagation path. This will reduce the uncertainty in the inversion which will become more severe as the bubble population becomes denser (e.g. in the surf zone) and more complex (e.g. with the existence of spikes (Feuillade, 1996). The operational procedure can be undertaken such that the combination-frequency result is examined first, such that the propagation tests solves a 'forward' problem (section 3.2.1); alternatively, the 'inverse' problem may be solved independent of the combination-frequency result, allowing the two techniques to be compared (section 3.2.2). The latter procedure, though the more difficult, will provide useful data on the limitations of the techniques, which have been independently used in the past to gather bubble data which is now part of the scientific record. It should be noted that the same data can be treated both ways, allowing effectively two results from a single sea trial.

Other factors have been incorporated to maximise the cost-effectiveness of the trials. As described above, the same acoustic pulse is used as the source for both tests. The first trials would employ horizontal array to test the two systems. On the assumption that, over distance scales of the order of a metre, the bubble population changes more with depth than in the horizontal direction, the propagation test will be examining an approximately constant bubble population along its length, a population which the combination frequency tests will also be measuring. However the second set of trials will use a more ambitious arrangement, yet one which again is optimised for cost-effectiveness.

The first arrangement places the ring transducer with its axis horizontal. Along that axis are spaced four hydrophones. As the ring transducer produces the multi-frequency pulse train of the form shown in Fig. 13 for use in the combination frequency measurement, those pulses propagate out and are detected by each hydrophone in turn. The propagation results can be used to confirm the bubble population measured by the ring transducer (section 3.1.1) or inverted to gain an independent measure of the population (section 3.1.2). The result can be discussed in terms of the horizontal uniformity of the bubble population. The main purpose, however, is to test the system for stage 2, the rig for which is shown in Fig. 19.

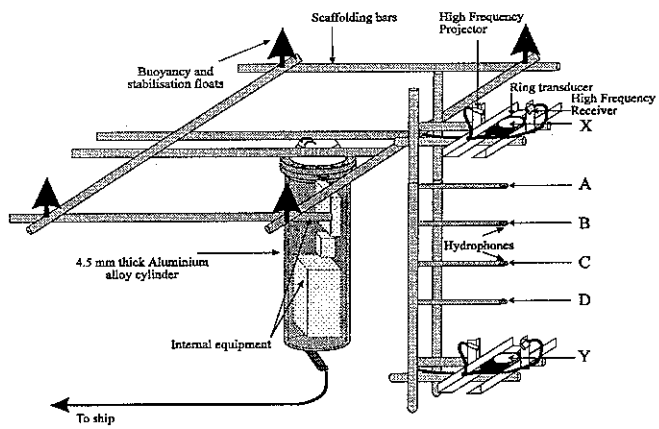

Fig. 19: Trial arrangement for simultaneous use of combination frequency (to provide a measure of the bubble population at one specific location) and a line array: two combination-frequency rigs provide ground-truthing at the start of propagation of pulses both in the upwards & downwards directions.

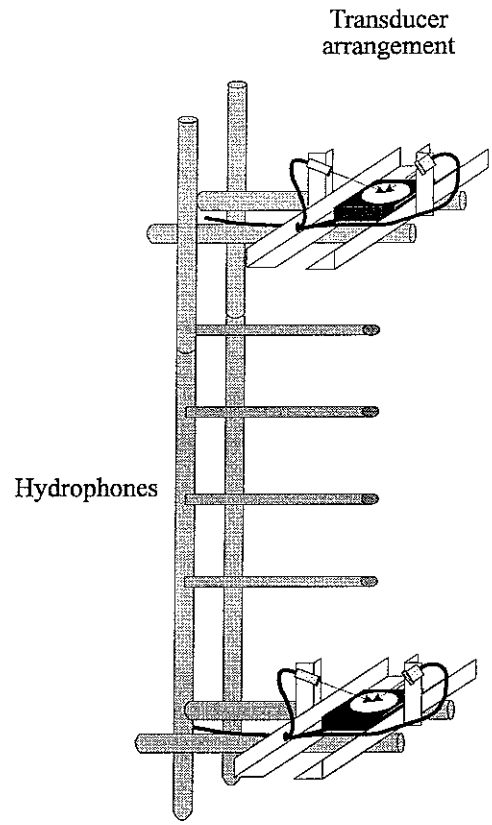

Fig. 20: Detail of the ring transducers and the line array.

That rig has the same cylinder geometry as will be used to mount the transducers when they were horizontal. Unlike the case described in section 2.4.2, the cylinder is suspended from a buoyed frame such that it is beneath the surface, reducing the invasiveness of the rig with respect to bubble entrainment. Two ring transducers, their axes now vertical (which may be preferable for minimising invasiveness with respect to bubble motions), are used, and the hydrophone arrangement spans the distance between them. The combination frequency tests are performed alternatively using the top, and then the bottom, ring transducer: If, as in section 2.4.2, the runs are made every 8 seconds (though it is hoped to reduce this time), then each ring transducer measures the bubble population at its centre once every 16 seconds, with the measurements staggered. The resulting protocol will therefore be as follows. At time $t = 0$ the top transducer will send out its multi-tone pulse, measuring the bubble population at the point marked X in Fig. 19 (this region is shown expanded in Fig. 20). The same pulse will propagate, being recorded in turn at hydrophones A, B, C and D. At time $t = 8$s, the lower ring transducer will send out its pulse, measuring the local population at point Y, and propagating a pulse upwards to be detected in turn by hydrophones D, C, B and A. At time $t = 16$s, the process beings again. Therefore every eight seconds we obtain propagation data up or down the water column, ground truthed for each run by a combination-frequency measurement at X or Y. By switching in this way, it will be possible to implement this technique will very little additional hardware.

Additional equipment will be required to transmit and acquire data from the four hydrophones used in the 'propagation' tests: the additional channels will also be used to measure the ambient noise generated by the breaking waves (with a degree of spatial

resolution being afforded by the line array). This can be interpreted in terms of the evolution of the bubble population, which is important for discussion of the gas flux (section 3.3). The extra channels will also be used for measurements of the water temperature, salinity and turbulence in the test region. Other measurements, including the air temperature and windspeed, and video and photographic records of the wavebreaking events, will be recorded from the ship.

3.2 Determination of the bubble population from the propagation characteristics

The bubble distribution function in a unit volume of water can be determined through an inverse method of calculation that relies on either the phase speed, or the attenuation, of an incident acoustic plane wave. The calculation is based on the resonance characteristics of the bubbles. This section outlines the forward process, i.e. calculation of the propagation characteristics from a given bubble population. The proposal is based on using both combination-frequency and propagation systems. Preliminary calculations were undertaken to illustrate the potential to undertake the measurement of the bubble population from the propagation characteristics. The relevant formulations were encoded, and bubble populations identical to those assumed by Commander and Prosperetti (1989) were inputted to the calculation. Comparison of the results validates the codification.

The authors then undertook propagation calculations based on an *a priori* bubble population obtained as detailed in section 2.4.2. Attenuation values at ten frequencies were taken from the field and used as the data for the inversion procedure. The ten attenuation values corresponded to the pump frequencies of the combination frequency transducer that were used to determine the original bubble distribution. The inverse method would be validated once the resulting bubble distribution resembled that obtained in the field from the combination frequency method.

3.2.1 Calculations employed for the forward problem

A published analysis involving linear pressure waves in liquids (Commander and Prosperetti, 1989) details the underlying physical concepts behind the calculation of the phase speed and attenuation of a plane wave travelling through a mono-disperse bubble population. As detailed in that paper, the extension of the equations to a fluid volume containing various numbers of bubbles at discrete radii intervals is straightforward. The principles of the calculation of attenuation and phase speed of a linear plane wave are as follows:

The squared ratio of the sound speed in a bubble-free volume of fluid to that in the bubble-populated fluid is given by the following equation.

$$\frac{c^2}{c_m^2} = 1 + \sum_{j=1}^{N} \frac{4\pi c^2 n\{a_j\}}{\omega_o^2 - \omega^2 + 2ib\omega} \qquad (3.1)$$

where c and c_m are the sound speeds of the acoustic plane wave in a bubble free and bubble populated fluid volume respectively. The term n represents the number of bubbles per unit volume; a_j is the equilibrium radius of a bubble within the j^{th} discrete range; b represents the damping, and is described in section 3.2.1(a), and ω and ω_o refer to the insonification frequency and the resonant frequency of the bubble (of radius a_j) respectively. The ratio is a complex one and can be set out as follows:

$$\frac{c}{c_m} = u - iv \tag{3.2}$$

The imaginary and real parts of this ratio are then used to determine the attenuation (A) and phase speed (V) from (3.3) and (3.4):

$$A = 20(\log_{10} e)\left(\frac{\omega v}{c}\right) \approx 8.6859\left(\frac{\omega v}{c}\right) \tag{3.3}$$

$$V = \frac{c}{u} \tag{3.4}$$

To ensure that these equations could be implemented properly, comparisons were made between the plots generated by Commander and Prosperetti for pre-defined bubble populations and those that were subsequently generated by the authors using customised Matlab routines. The bubbles populations presented by Commander and Prosperetti were characterised through the equilibrium radii and the void fractions (β). In order that void fractions could be translated into values of n, the following relationship was used:

$$\beta = \frac{4}{3}\pi R^3 n \tag{3.5}$$

3.2.1(a) Definition of the variables

Equations (3.1) and (3.3) are dependant on three variables. The first to be described here is the damping constant, b;

$$b = \frac{2\mu}{\rho a^2} + \frac{p_o}{2\rho a^2 \omega}\Im\Phi + \frac{\omega^2 a}{2c} \tag{3.6}$$

The three terms in this expression relate to the viscous, thermal and acoustic damping of an oscillating bubble respectively. The term μ represents the shear viscosity of the fluid, p_o is the equilibrium pressure within the bubble and ρ is the density of the fluid surrounding the bubble. The scaling factor Φ is related to the polytropic index (introduced in equation 1.1), and as such incorporates the thermal damping. It is defined as:

$$\Phi = \frac{3\gamma}{1 - 3(\gamma - 1)i\chi\left[(i/\chi)^{\frac{1}{2}}\coth(i/\chi)^{\frac{1}{2}} - 1\right]} \tag{3.7}$$

where χ is given by:

$$\chi = \frac{D}{\omega a^2} \tag{3.8}$$

where D is the thermal diffusivity of the gas within the bubble. Throughout this formulation, the resonant frequency of the bubble was calculated from:

$$\omega_o^{2\sim} = \frac{p_o}{\rho a^2}\left(\Re\tilde{\Phi} - \frac{2\sigma}{ap_o}\right) \tag{3.9}$$

where σ is the surface tension of the bubble wall.

3.2.1(b) Assigned values

Many of the variables in the above equations were not dependant on the insonification frequency or the bubble radius. An initial distinction had to be made between the use of sea water variables or pure water variables. The work that was presented by Commander and Prosperetti detailed acoustic behaviour in the lab and so used pure water. Values that would change in 'dirty' oceanic water are presented here in brackets after the values for pure water (Leighton, 1994 p.120):

$c = 1450$ ms^{-1};
$p_o = 1$ atm $= 101325$ Nm^{-2};
$\sigma = 7.2\times10^{-2}$ Nm^{-1} (3.6×10^{-2} Nm^{-1});
$\mu = 0.001$ Ns/m^2;
$D = 2.08\times10^{-5}$ ms^{-1} (For air under 1 atm. pressure);
$\gamma = 1.4$;
$\rho = 1000$ kgm^{-3} (1027.34 kgm^{-3}).

3.2.1(c) Comparison between models

The models that were presented by Commander and Prosperetti were graphically compared to those that were generated from a customised model created using Matlab by the authors. This section presents these figures, and serves to validate the simulations of a mono-disperse bubble population, a bi-disperse population and finally a population that was calculated from the use of the combination frequency technique in the field (Fig. 17).

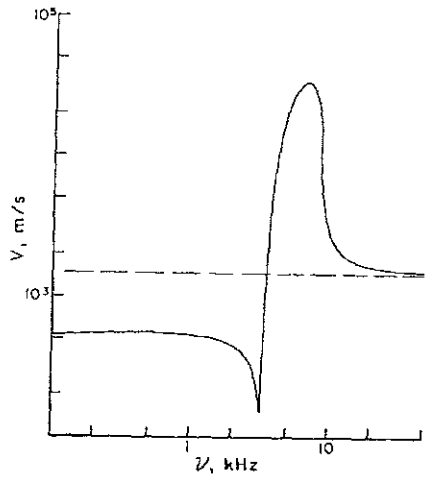

Fig. 21: Phase speed of pressure waves against insonification frequency given for a mono-disperse bubble population with a radius of 0.994 mm and a void fraction of 0.0377% from Commander and Prosperetti

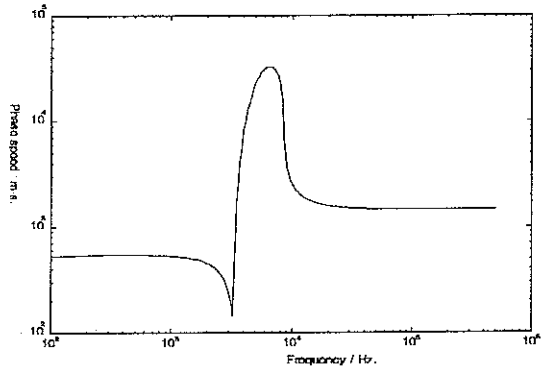

Fig. 22: A simulated model of the phase speed of pressure waves against insonification frequency of pressure waves in a fluid volume identical to that of Fig. 21, using Matlab. The plot demonstrates the bubble pulsation phase and the bulk modulus argument.

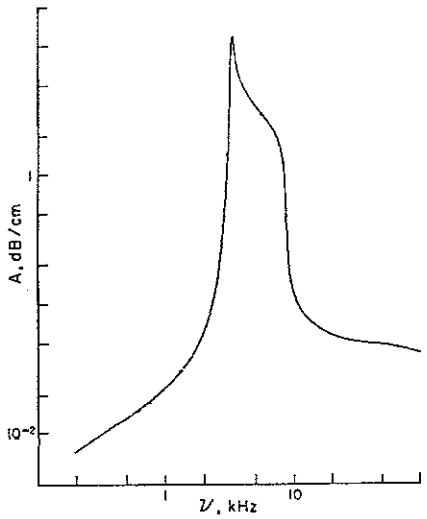

Fig. 23: The attenuation coefficient for a bubble radius of 0.994 mm and a void fraction of 0.0377% from Commander and Prosperetti.

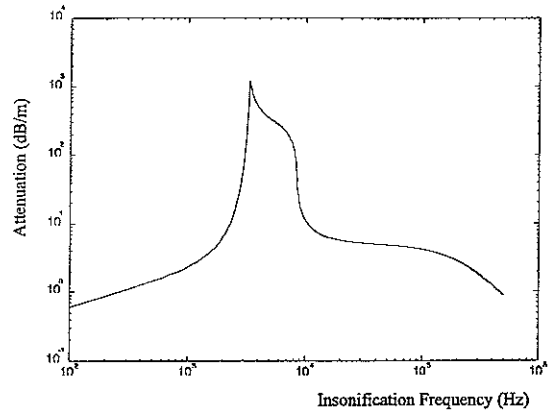

Fig. 24: A simulated model of the attenuation coefficient against insonification frequency of pressure waves in a fluid identical to that of Fig. 23, using Matlab. The attenuation demonstrates a maximum at the resonant frequency of the bubble. When the bubble resonates the scattering cross sectional area is a maximum.

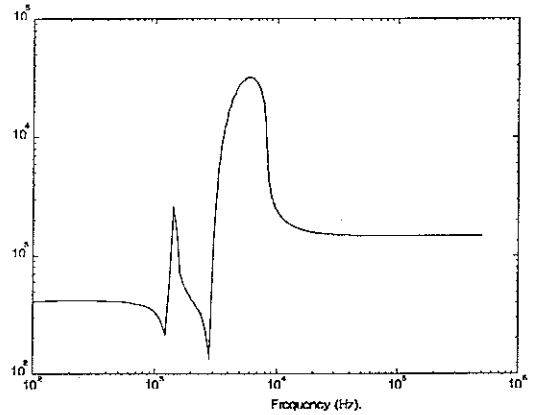

Fig. 25: Phase speed of pressure waves against insonification frequency given for a bi-diperse bubble population with a radius of 1.13 mm and a void fraction of 0.0421% and a radius of 2.53 mm with a void fraction of 0.0256%, from a simulation in Matlab. No comparison available from Commander and Prosperetti, 1989.

Comparing the frequency dependence of both phase speed (Figs. 21 and 22) and attenuation (Figs. 23 and 24) predicted by the codes of Commander and Prosperetti, and those developed at ISVR, suggests that for the monodisperse population tested here, the models agree well. The ISVR code was then used to study a bi-disperse bubble population (Fig. 25). The plot shows the expected double-resonance behaviour: Below its resonance, a bubble pulsates in phase with the sound field and therefore reduces the sound speed through increasing the compressibility; but the phase changes at resonance can cause it to effectively increase the compressibility of bubbly water over that of bubble-free water.

However, Commander and Prosperetti did publish plots of the frequency-dependent attenuation for this bi-disperse bubble population (Fig. 26) This can be seen to agree well with the result of the ISVR calculations (Fig. 27).Finally, a bubble population was selected (Fig. 28) from the data measured by the author and co-workers (as described in section 2.4.2). This data was then inputted into the ISVR code and used to predict the frequency-dependent phase speed (Fig. 29) and attenuation (Fig. 30).

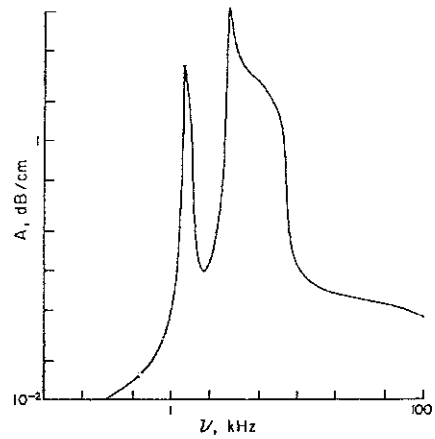

Fig. 26: The attenuation coefficient for water containing bubbles with a radius of 1.13 mm and a void fraction of 0.0421% together with a population of bubbles with a radius of 2.53 mm and a void fraction of 0.0256%, from Commander and Prosperetti, 1989.

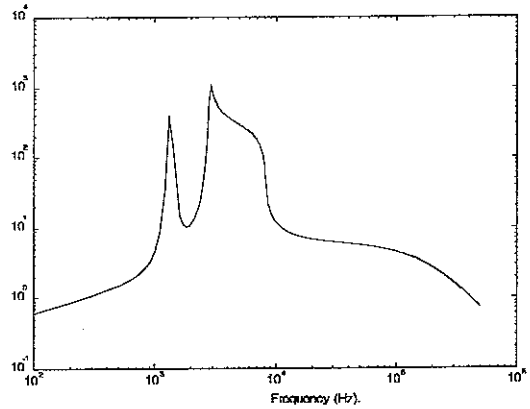

Fig. 27: The attenuation coefficient for water containing bubbles with a radius of 1.13 mm and a void fraction of 0.0421% together with a population of bubbles with a radius of 2.53 mm and a void fraction of 0.0256%, from a simulation in Matlab.

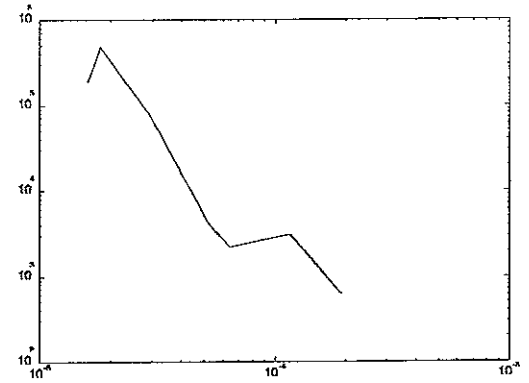

Fig. 28: A plot of the distribution function of the bubbles in the Solent at a depth of 0.50 m acquired using the combination technique.

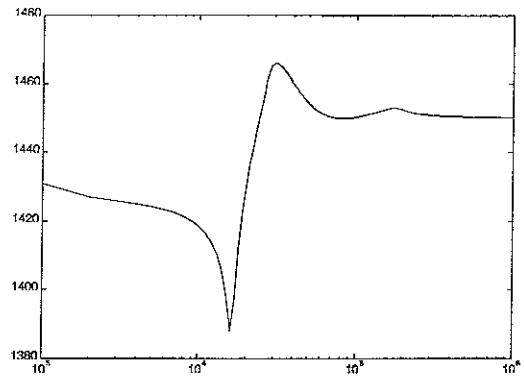

Fig. 29: The simulated phase speed of a linear plane wave incident on a volume of water containing the bubble distribution shown in Fig. 28, using Matlab.

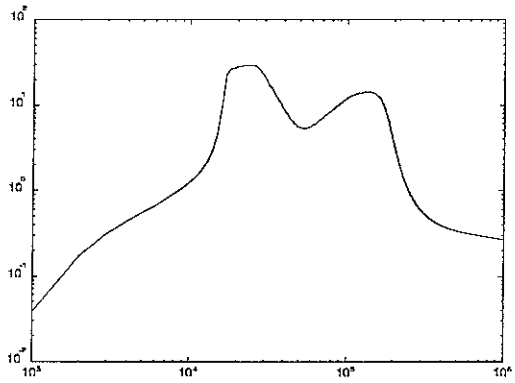

Fig. 30: The simulated attenuation coefficient of a linear plane wave on a volume of water containing the bubble distribution shown in Fig. 28, using Matlab.

Figs. 29 and 30 show that, in the planned sea test with a horizontal array, the bubble population (as measured at one point by the combination frequency technique) can be used to predict the likely phase speed and attenuation which the linear array will measure. Comparison of the measure propagation characteristics will allow cross-validation of the techniques, and an assessment of the differences between the point-measurement of the combination-frequency tests, and the measurement form the line array, which effectively integrates the bubble population across three co-linear, adjacent, 10 cm paths. Such tests are important for preparation for the second set of trials, where: first, the line array examines a bubble population which changes along its length (i.e. with depth), ground-truthed at top and bottom by combination-frequency systems; and second, the propagation data is inverted to give the bubble population.

3.3 Oceanographic applications of the results

The bubble size distribution is an important influence with respect to the bubble-mediated gas flux, and vice versa. Examining both 'clean' and 'dirty' bubbles (see later), Thorpe (1982) concluded that rate of change of size of oceanic bubbles everywhere except very close to the surface is likely to be controlled by diffusive

processes and not Boyle's Law. Therefore it is diffusion which is likely to control the size distribution of bubbles in the sea. Compared with the equilibrium gas flux for a plane atmosphere/ocean interface, large bubbles contribute additional surface area, whereas in small bubbles the Laplace pressure shifts the equilibrium towards increased dissolution. A similar effect results from hydrostatic pressure, which acts on all bubbles regardless of size, but which will also alter the equilibrium bubble size. Clearly the size distribution of bubbles in a population influences gas dissolution and exsolution. The importance of including the effect of small bubbles in any such consideration is illustrated by a cumulative calculation of the gas contained within bubbles (Fig. 31).

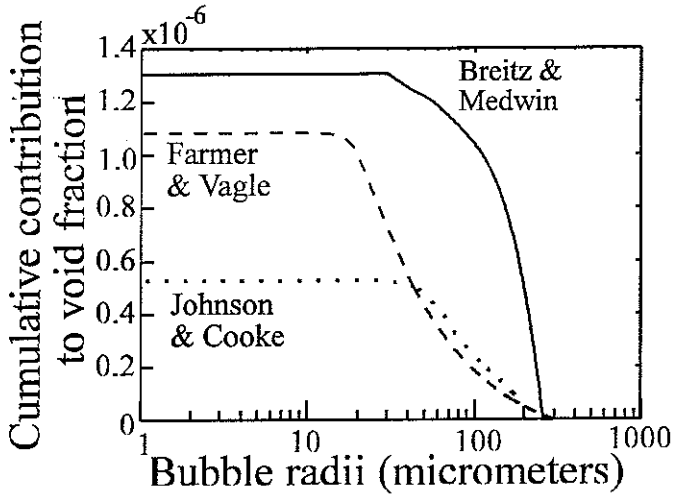

Fig. 31: The cumulative contribution (of estimates of the bubble radii) to the eventual void fraction from integration of the oceanic bubble population data of Breitz & Medwin (1989, unbroken), Farmer & Vagle (1989, dashed) and Johnson & Cooke (1979, dotted).

The calculation was made up to 200 kHz since integration (Leighton *et al.*, 1996) of bubble size densities from three surveys yields total gas void fractions (as shown in Fig. 21) of 1.3×10^{-6} (Brietz and Medwin, 1989), 1.1×10^{-6} (Farmer and Vagle, 1989), and, from the only optical survey of the three, 0.5×10^{-6} (Johnson and Cooke, 1979). To measure 95% of the void fraction that each survey did in fact measure, the minimum bubble radius each survey would have to measure would be 43 μm for both Brietz and Medwin (1989) and Johnson and Cooke (1979), but 18 μm for Farmer and Vagle (1989), the survey which revealed a peak in the population at around 20 μm radius. To measure this lowest estimate of the minimum radius would require a resonant pump frequency of 200 kHz.

It can be seen, therefore, that the existence of a peak in the bubble population has an important influence on calculations involving the gas content of the oceanic bubble population. We have confidence in the peak in the population at 18 μm, demonstrated in Fig. 17. This peak is evident on each of the six tests performed, and so is demonstrably a legitimate property of the local bubble population. Indeed, there is very little variation in the average population over the entire radius range measured over the six tests. The appearance of this peak is a contentious point - the most recent historical population measurement using the flat plate acoustic resonator technique (Farmer and Vagle, 1997) does not show this peak, only a flattening of the number of

bubbles per micrometer radius range as the radius becomes less. However, from a consideration of the mechanisms of bubble fragmentation, a peak in the spectrum should be expected. The ambient population of small bubbles which persist over many 100s of seconds (the so-called 'old-age' population) arises though the fragmentation of larger bubbles which are caught in oceanic shear currents and the high amplitude (and therefore unstable) pulsations which follow entrainment. However, as a bubble becomes smaller, the effect of the surface tension around the wall becomes more and more important in determining its stability - for a 1 mm bubble, these Laplace surface tension forces account for around 0.1 % of the internal pressure of a non-pulsating bubble at atmospheric pressure, but these rise to ~ 8 % for a 16 μm bubble. These forces determine the ease by which a bubble can deform its shape from a sphere, and therefore also the probability by which a shape oscillation can lead on to bubble fragmentation. Thus, the potential for a bubble to fragment decreases the smaller it becomes, and a maximum in the bubble population may result.

It is intended that, during any future work, a theoretical examination be made of the processes of fragmentation, buoyancy and dissolution, adding fragmentation to the earlier studies of the interaction between the bubbles' size, position, velocity and gas flux (Thorpe, 1982). The fragmentation theory will be based on that of Longuet Higgins (1992), who began with a one-dimensional, probabilistic model of bubble fragmentation, then extended it to two and three dimensions. The one-dimensional model (which might, for example, model the break-up of a cylindrical air pocket trapped beneath a plunging breaker) considers a line segment of unit length, which is divided by m points spaced randomly into $m+1$ subsegments of typical length X. The probability $p(X)$ of the length of this subsegment is:

$$p(X) = m(1-X)^{(m-1)} \qquad \text{(provided } 0 < X < 1 \text{ and } m > 1\text{)} \qquad (3.10)$$

and the cumulative probability function $P(X)$ is given by:

$$P(X) = \int p(X)dX \qquad (3.11)$$

The derivative of the cumulative probability function $P(X)$ with respect to $\ln(X)$ gives the density of the distribution:

$$\frac{dP}{d\{\ln(X)\}} = \frac{dP}{dX}\frac{dX}{d\{\ln(X)\}} = p(X)X = m(1-X)^{(m-1)}X \qquad (3.12)$$

Replacing the line segment of unit length, divided by m points, by a block of unit volume, divided by m parallel planes, the probability density of the sub-blocks will be exactly the same as shown above.

If R denotes the radius of a spherical bubble of volume V and R_0 the radius of a bubble (of volume V_0 which is equal to unity), the density of the distribution of bubble radii is given by:

$$\frac{dP}{d\{\ln(R)\}} = \frac{dP}{dV}\frac{dV}{d\{\ln(R)\}} = p(V).3V = m(1-V)^{(m-1)}3V \qquad (3.13)$$

In the two-dimensional model a cubical block of unit volume, which is split by two sets of perpendicular and independent planes, is considered. The distributions are calculated using numerical integration. In a similar way the model can be extended to three dimensions, with distributions having a much more negative mean. In all three cases the distributions for a large number of planes tend to limiting values of non-zero standard deviation and skewness. The results of preliminary tests, by the author and co-workers, on the suitability of this theory for such a study are shortly to be published (Leighton *et al.*, 1998).

Given that the smallest bubbles are an issue, then the model must incorporate stabilising factors which exist in the sea. Unlike the effect of hydrostatic pressure, the tendency of surface tension to cause bubbles to dissolve is very much influenced by the chemical state of the water. A real bubble is rarely so simple an entity as a gas pocket, and in addition to the gas and the bulk liquid its surface is likely to have complex properties of its own. Most water samples (domestic, industrial and in the natural world) will contain surface active materials, and bubbles rapidly absorb these onto their walls (Clift *et al.*, 1978). As a result, the wall can sustain a stress. Once the material covers the bubble its translational dynamics do in fact tend to those of a rigid particle because of the immobilisation of the interface and the resulting viscous boundary layer on the bubble. Bubbles whose dynamics are significantly affected by surface-active materials in the wall are termed 'dirty bubbles'. Those possessing no surface-active material are called 'clean bubbles'. In general in the natural world, and particularly in the ocean, clean bubbles of radii less than ~ 100 μm become 'dirty' in a few tens of seconds. Whilst the surface tension, σ, equals 7.2×10^{-2} N/m for clean bubbles in water, the walls of dirty bubbles in the ocean may have surface tension reduced to typically 3.6×10^{-2} N/m (Thorpe, 1982; Clift *et al.*, 1978).

The wall of a clean bubble is mobile: even if the bubble as a whole is not moving, the various fluid elements within the wall can flow relative to one another. This mobility means that the constraint that applies to rigid spheres, that the fluid velocity tangential to the surface must be zero at the sphere's surface, is not applicable to the clean bubble. Motion at the interface drives internal circulation of the gas contents within the bubble. If the bubble is dirty, surface contaminants immobilise the interface, affecting the flow field on either side of it: internal circulation within the bubble is reduced or eliminated, and the effect on the liquid flow field outside the bubble changes the dynamics, so that for example small dirty bubbles translate as rigid spheres. If an initially clean bubble moves through a medium containing surface-active agents, these substances will tend to accumulate at the liquid/gas interface. Consequently a translating bubble will tend to collect surface-active material from the liquid through which it is moving. These substances are swept to the rear of the bubble, and the concentration gradient so set up will create tangential stresses in the bubble wall as the surface tension varies from the front to the rear of the bubble. These stresses will make the interface rigid.

Since the presence of surface-active entities in the water can significantly alter the circulation of the gas within the bubble, studies relevant to the ocean should simulate the complex chemical character of seawater. The cleanliness of the bubble is very important to the gas flux (Woolf and Thorpe, 1991; Memery and Merlivat, 1985), dirty bubbles being generally more efficient at transferring gas into the ocean. Bubbles formed in salt water tend to be more numerous, particular regarding the smallest bubbles (Scott, 1975), and are less prone to coalesce than bubbles in fresh water (Zieminski *et al.*, 1976). Both effects are suggestive of a stabilising skin at the bubble wall.

There are two common models for explaining the anomalous persistence of bubbles, both of which involve the introduction of other agents to stabilise against dissolution (Leighton, 1994, §2.1). First, gas pockets may be stabilised against dissolution by solid structures in crevices and cracks in free-floating particles within the liquid [Harvey, 1944; Leighton, 1994, §2.1; 1998; Atchley and Prosperetti, 1989), or by biological structures (Leighton *et al.*, 1995).

Second hydrophobic impurities (such as fatty acid) can stabilise air bubbles in water These accumulate on the wall of a bubble, and as the bubble dissolves, the area of the bubble wall becomes smaller, and at some point the organic impurities will form a complete 'skin' surrounding the bubble. Further decrease in bubble size is inhibited by this skin: a decrease in bubble wall area would necessitate a decrease in the configurational entropy of the skin. The model was first proposed by Fox and Herzfeld (1954) who envisaged a rigid skin of organic compounds. Herzfeld subsequently withdrew the model as being inconsistent with the measurements of Strasberg (1959), and Barger (1964) failed to find any experimental evidence. Sirotyuk (1970) modified the model to incorporate a skin of specially orientated surface-active polar molecules. The restriction of a rigid skin was removed. Akulichev (1966) proposed a model where ionic charges present in the liquid migrate to the surface and bring about stabilisation through Coulomb repulsion. The most successful of these 'skin' models was put forward by Yount and co-workers (1982, 1984), who proposed an elastic organic surface-active skin which, though initially permeable to gas, became impermeable as the concentration of organic molecules increased on the contracting bubble wall, thus stabilising the bubble against dissolution. This variably-permeable skin allows the model to give results compatible with observations of gas diffusion (Lieberman, 1957), rectified diffusion and Strasberg's (1959) observations on the effects of hydrostatic pressure and degassing. The surface-active molecules are stored in a reservoir located just outside the skin. Molecules can be exchanged between the skin and the reservoir as required when the volume of the bubble, and therefore the area of the bubble wall, changes. Thus, unlike ordinary gas bubbles, Yount's nuclei can be subjected to changes in pressure and stabilised at several different pressures, providing that the threshold for bubble formation is not exceeded. This fact can be used to distinguish such stabilised nuclei from ordinary gas bubbles (Yount *et al.*, 1984). Yount's model is in agreement with the observations of Johnson and Cooke (1979), who noted that some bubbles, when injected into sea water, after a certain time ceased to dissolve any more (others dissolved altogether).

Incorporation of such factors as fragmentation and stabilisation in models of dissolving oceanic bubbles are necessary: the bubbles which persist the longest tend to

be the smallest ones, those on which the buoyant forces are weakest. In the absence of stabilising mechanisms, it is on such bubbles that the Laplace forces, which tend to cause dissolution, are the most potent. Additionally, where buoyancy is weak on such small bubbles, they will tend to reach to the greater depths, so affecting the influence of hydrostatic forces on the gas flux.

4. CONCLUSIONS

This report details two sea trials where the combination-frequency technique was used to measure oceanic bubble populations, and compares the results with historical data. The report then discusses the future direction the study might take. This would involve the development and deployment of a system for measuring the bubble population through the water column. In addition existing theory would be modified to incorporate these bubble size distributions into the discussion of the atmosphere/ocean mass flux.

5. REFERENCES

Akulichev V.A. 1994. Cavitation nuclei and thresholds of acoustic cavitation in ocean water, in *Bubble Dynamics and Interface Phenomena, Proceedings of an IUTAM Symposium (Birmingham, 6-9 Sept. 1993), J.R. Blake, J.M. Boulton-Stone and N.H. Thomas, eds.,* Kluwer Academic Publishers, The Netherlands, 171-178, 1994

Akulichev VA. 1966. Hydration of ions and the cavitation resistance of water. *Sov Phys Acoust,* **12**: 144-149

Atchley A.A., Prosperetti A. 1989 The crevice model of bubble nucleation. *J. Acoust. Soc.* Am., **86,** 1065-1084.

Barger J. 1964. Acoust Res Lab, Harvard Uni, Tech Memo No 57, April 1964

Belcher E.O. 1980. Quantification of bubbles formed in animals and man during decompression, *IEEE Trans. Biomed. Eng.*, **27**, 330-338.

Blanchard DC, Woodcock AH. 1957. Bubble formation and modification in the sea and its meteorological significance. *Tellus*; **9**:145-158

Breitz N, Medwin H. 1989. Intrumentation for in situ acoustical measurements of bubble spectra under breaking waves. *J Acoust Soc Am*; **86**:739-743

Buckingham M.J. and Epifanio, C.L. 1997. Bubbles nd breaking waves: Imaging in space, time and frequency. Natural Physical Processes associated with Sea Surface Sound (T.G. Leighton, editor), University of Southampton, 39-44

Buckingham, M.J. 1991. On acoustic transmission in ocean-surface waveguides, *Phil. Trans. R. Soc. Lond.* **335**, 513-555.

Clift R, Grace JR, Weber ME. Bubbles, Drops and Particles. Academic Press. 1978

Crum L.A. and Mao Y. 1996 Acoustically enhanced bubble growth at low frequencies and its implications for human diver and marine mammal safety, *J. Acoust. Soc. Am.*, **99**, 2898-2907

Detsch, R.M. & Sharma, R.N. The critical angle for gas bubble entrainment by plunging liquid jets. *The Chemical Engineering Journal* (1990) 157-166.

Detwiler A , Blanchard DC. 1978. Ageing and bursting bubbles in trace-contaminated water. Chem Engng Sci; **33**: 9-13

Eller A.I.. 1970. Damping constants of pulsating bubbles, *J. Acoust. Soc. Am.* **47**, 1469-1470

Farmer D.M. and Vagle S. 1997. Bubble measurements using a resonator system, in *Natural physical processes associated with sea surface sound*, T.G. Leighton, Ed. Southampton, UK: University of Southampton, 1997, 155-162.

Farmer DM, Vagle S. 1989. Waveguide propagation of ambient sound in the ocean-surface bubble layer. *J Acoust Soc Am*; **86**: 1897-1908

Feuillade C. 1996. The attenuation and dispersion of sound in water containing multiply interacting air bubbles, *J. Acoust. Soc. Am.*,. **99**, 3412-3430.

Fox FE, Herzfeld KF. 1954. Gas bubbles with organic skin as cavitation nuclei. *J Acoust Soc Am*, **26**: 984-989

Greenspan, M. and Tschiegg, C.E. 1967 Radiation-induced acoustic cavitation; apparatus and some results. *J. Res. natl. Bur. Stand.,* Section C, **71,** 299-311.

Harvey, E.N., Barnes, D.K., McElroy, W.D., Whiteley, A.H., Pease, D.C. and Cooper, K.W. (1944) Bubble formation in animals. *J. Cell Comp. Physiol.,* **24,** 1-22.

Herring C. 1941. Theory of the pulsations of the gas bubble produced by an underwater explosion, Report No. 236, *OSRD*, 1941.

J.Y. Chapelon, P.M. Shankar and V.L. Newhouse. 1985. Ultrasonic measurement of bubble cloud size profiles, *J. Acoust. Soc. Am.*, **78**, 196-201,.

Johnson BD and Cooke RC. 1979. Bubble populations and spectra in coastal waters: a photographic approach. *J. Geophys. Res.*; **84**, C7: 3761-3766

Keller J.B. and Miksis M. 1980. Bubble oscillations of large amplitude, *J. Acoust. Soc. Am.*, **68**, 628-633.

Koller D., Li Y., Shankar P.M. and Newhouse V.L. 1992. High speed bubble sizing using the double frequency technique for oceanographic applications, *IEEE J. Oceanic Eng.*, **17**, 288-291.

Kolovayev PA. 1976. Investigation of the concentration and statistical size distribution of wind produced bubbles in the near-surface ocean layer. *Oceanology*; **15**: 659-661

Leighton T.G. (editor), 1997. *Natural Physical Processes Associated With Sea Surface Sound*, University of Southampton, 1997.

Leighton T.G. 1994. Acoustic Bubble Detection. I. The detection of stable gas bodies, *Environmental Engineering*, **7**, 9-16.

Leighton, T.G. 1994. *The Acoustic Bubble*, Academic Press, London.

Leighton T.G. 1998. The principle of cavitation, Chapter 9, *In: ed. T A Mason and G Povey, Ultrasound in Food Processing*, Blackie Academic and Professional (in press).

Leighton, T.G., White, P.R., Marsden, M.A. 1995 Applications of one-dimensional bubbles to lithotripsy, and to diver response to low frequency sound, *Acta Acustica,* **3**, 517-529.

Leighton T.G., Phelps A.D. and Ramble D.G. 1996. Bubble detection using low amplitude multiple acoustic techniques, in *Proceedings of the 3rd European Conference on Underwater Accoustics*, J.S. Papadakis, Ed. Crete, Greece: FORTH-IACM, 1996, 1143-1148.

Leighton T.G., Phelps A.D. and Ramble D.G.,1997. Measurement of the bubble population in coastal waters using combination frequencies of MHz order,

Proceedings of the NATO conference on High frequency acoustics in shallow water, Lerici (Pace, NG, Pouliquen E, Bergem O, and Lyons, AP, eds.), 1997, 305-312

Leighton T.G., White P.R. and Schneider M.F. 1998. The detection and dimension of bubble entrainment and comminution. *J. Acoust. Soc. Am.* (in press).

Lieberman L. 1957. Air bubbles in water. *J Appl Phys*, **28**: 205-217

Longuet-Higgins M.S. 1990. Bubble noise spectra, *J. Acoust. Soc. Am.*, **87**, 652-661.

Longuet-Higgins M.S. (1992). The crushing of air cavities in a liquid," *Proc. R. Soc. Lond.* **439**, 611-626

MacIntyre F. 1986. On reconciling optical and acoustic bubble spectra in the mixed layer. In: Oceanic whitecaps and their role in air-sea exchange processes. Monanhan EC, O'Muircheartaigh I, eds. D. Reidel Pub. Co., Dordrecht, Holland, 1986; 95-100.

Medwin H and Breitz ND. 1989. Ambient and transient bubble spectral densities in quiescent seas and under spilling breakers. *J Geophys Res*; **94**:12751-12759

Medwin H. 1977. In situ acoustic measurements of microbubbles at sea. *J Geophys Res*: **82**: 971-976

Melville W.K., Terrill E. and Veron F. 1997. Bubbles and turbulence under breaking waves, in *Natural physical processes associated with sea surface sound*, T.G. Leighton, Ed. Southampton, UK: University of Southampton, 135-146.

Memery, L. and Merlivat, L. 1985. Modelling of gas flux through bubbles at the air-water interface. *Tellus*; **37B**: 272-285

Minnaert M.. 1933. On musical air-bubbles and the sounds of running water, *Phil. Mag.*, **16**, 235-248.

Neppiras E.A.. 1980. Acoustic cavitation, *Physics Reports* **61**, 159-251

Newhouse V.L. and Shankar P.M. 1984. Bubble sizing using the nonlinear mixing of two frequencies, *J. Acoust. Soc. Am.*, **75**, 1473-1477.

Peregrine D.H. and Prentice, P.R. 1994. Jet formation at a free surface, in *Bubble Dynamics and Interface Phenomena, Proceedings of an IUTAM Symposium (Birmingham, 6-9 Sept. 1993), J.R. Blake, J.M. Boulton-Stone and N.H. Thomas, eds.,* Kluwer Academic Publishers, The Netherlands, 397-404, 1994

Phelps A.D. and Leighton T.G. 1996. High resolution bubble sizing through detection of the subharmonic response with a two frequency technique, *J. Acoust. Soc. Am.*, vol **99**, 1985-1992

Phelps A.D. and Leighton T.G. 1997. Measurement of bubble populations near the sea surface using combination frequencies: adaptation and calibration of device between two sea trials, in *Natural physical processes associated with sea surface sound*, T.G. Leighton, Ed. Southampton, UK: University of Southampton, 1997, 198-210.

Phelps A.D., Ramble D.G. and Leighton T.G. 1997. The use of a combination frequency technique to measure the surf zone bubble population, *J. Acoust. Soc. Am.*, **101**, 1981-1989

Phelps A.D. and Leighton T.G. 1998. Oceanic bubble population measurements using a buoy-deployed combination frequency technique. In preparation for IEEE J. Ocean Engineering.

Pumphrey H.C. and Elmore P.A. 1990. The entrainment of bubbles by drop impacts, *J. Fluid Mech.,* **220**, 539-548

Scott JC. 1975. The role of salt in whitecap persistence. *Deep Sea Res*, **22,** 653-657

Scrimger J.A., Evans D.J., McBean G.A., Farmer D.M. and Kerman B.R. 1987. Underwater noise due to rain, hail and snow, *J. Acoust. Soc. Am.,* **81**, 79-85, 1987

Shankar P.M., Chapelon J.Y. and Newhouse V.L. 1986. Fluid pressure measurement using bubbles insonified by two frequencies, *Ultrasonics*, **24**, 333-336

Sirotyuk MG. 1970. Stabilisation of gas bubbles in water. *Sov Phys Acoustics,* **16**: 237-240

Strasberg M. 1959. Onset of ultrasonic cavitation in tap water. *J Acoust Soc Am,* **31**: 163-176

Su MY, Ling SC, Cartmill J. Optical measurements in the North Sea. In: Sea surface sound ed Kerman B (Kluwer, Dordrecht, 1988)

Thorpe S.A. 1982. On the clouds of bubbles formed by breaking wind-waves in deep water, and their role in air-sea gas transfer. *Philos. Trans. R Soc London.* **A 304**: 155-210

Thorpe SA. 1984. The role of bubbles produced by breaking waves in super-saturating the near-surface ocean mixing layer with oxygen. *Annales Geophysica*, **2**: 53-56

Tickner, E. G. Precision microbubbles for right side intercardiac pressure and flow measurements. In: *Contrast Echocardiography, Meltzer, R. S., Roeland, J. (eds.)*, (Nijhoff, London). (1982)

Walsh AL and Mulhearn PJ. 1987 Photographic measurements of bubble populations from breaking waves at sea. *J Geophys Res*; **92**: 14553-14656

Wenz, G.M. 1962. Acoustic ambient noise in the ocean: spectra and sources, *J. Acoust. Soc. Am.*, **34**, 1936-1956

Woolf DK and Thorpe SA. 1991. Bubbles and the air-sea exchange of gases in near-saturation conditions. *J Marine Res.* **49**: 435-466

Yount D E, Gillary E W, and Hoffman D C. 1984. A microscopic investigation of bubble formation nuclei. *J Acoust Soc Am,* **76**: 1511-1521

Yount DE.. On the evolution, generation, and regeneration of gas cavitation nuclei. *J Acoust Soc Am* 1982; **71**: 1473-81

Zieminski SA, Hume RM, Durham R. 1976. Rates of oxygen transfer from air bubbles to aqueous NaCl solutions at various temperatures. *Mar. Chem.*, **4**: 333-346